

Performance, Power, and Area Design Trade-offs in Millimeter-Wave Transmitter Beamforming Architectures

Han Yan, *Student Member, IEEE*, Sridhar Ramesh, Timothy Gallagher, Curtis Ling,
and Danijela Cabric, *Senior Member, IEEE*

Abstract—Millimeter wave (mmWave) communications is viewed as the key enabler of 5G cellular networks due to vast spectrum availability that could boost peak rate and capacity. Due to increased propagation loss in mmWave band, transceivers with massive antenna array are required to meet link budget, but their power consumption and cost become limiting factors for commercial systems. Radio designs based on hybrid digital and analog array architectures and the usage of radio frequency (RF) signal processing via phase shifters have emerged as potential solutions to improve radio energy efficiency and deliver performances close to conventional digital antenna arrays. In this paper, we provide an overview of the state-of-the-art mmWave massive antenna array designs and comparison among three array architectures, namely digital array, partially-connected hybrid array (sub-array), and fully-connected hybrid array. The comparison of performance, power, and area for these three architectures is performed for three typical 5G downlink use cases, which cover a range of pre-beamforming signal-to-noise-ratios (SNR) and multiplexing regimes. This is the first study to comprehensively model and quantitatively analyze all design aspects and criteria including: 1) optimal beamforming precoder, 2) quantization accuracy in digital-to-analog converter (DAC) and phase shifters, 3) local oscillator signal (LO) and RF signal distribution losses, 4) power and area based on state-of-the-art mmWave circuits including high-speed DACs, mixers, phase shifters, and power amplifiers. The analysis shows that the hybrid architecture provides marginal, if any, benefits over the digital array architecture. It also reveals that sub-array architecture suffers from reduced beamforming gain due to array partitioning, which has to be compensated with additional transmission power and signal processing. Fully-connected hybrid architecture is limited by significant RF signal distribution loss and corresponding cost of RF amplifiers needed to compensate this loss.

I. INTRODUCTION

Millimeter-wave (mmWave) communications is a promising technology for the future fifth-generation (5G) cellular network [1], [2]. In the US, the Federal Communications Commission (FCC) has voted to adopt a new Upper Microwave Flexible Use service in the licensed bands, namely 28GHz (27.5-28.35GHz band), 37GHz (37-38.6GHz band), 39GHz (38.6-40GHz) with a total 3.85GHz bandwidth [3]. The abundant spectrum facilitates key performance indicators (KPI) of 5G, including 10Gbps peak rate, 1000 times higher

traffic throughput than the current cellular system [4]. As shown in theory and measurements, mmWave signals suffer higher free-space transmission loss [5], and is vulnerable to blockage [6]. As a consequence, radios require beamforming (BF) with large antenna arrays at both base station (BS) and user equipment (UE) to combat severe propagation loss [7]. Besides, since the reliable communication range is much shorter, mmWave BSs will be deployed in an ultra-dense manner with inter-site distance in the order of hundred of meters [8], [9]. Due to these facts, performance, energy, and cost efficiency in the future mmWave base station (BS) radios become more important than ever before.

Implementations and deployments of transceiver arrays in sub-6GHz have shown a great success. In the 4G Long Term Evolution Advanced (LTE-A) system, BS supports up to 8 antennas [10] and arrays with even larger size are being actively prototyped [11] and will be soon available in the LTE-A PRO (the pre-5G standard). Those systems exclusively have digital array architecture based on a dedicated radio-frequency transceiver chain, with data converter and up/down-conversion, per each antenna, and rely on digital baseband for array processing. Many implementation challenges arise in scaling up array size [12] by an order of magnitude or more required for mmWave bands. System designers are also concerned about the high cost and power consumption in digital array architecture with massive number of RF-chains and ultra-wide processing bandwidth [13].

Recently, an emerging concept of hybrid array has been proposed. A hybrid array uses two stage array processing. The analog beamforming implemented with variable phase shifters (PS) provides beamforming gain and the digital beamforming in the baseband provides flexibility for multiplexing multiple user streams [14], [15]. As a result, hybrid array supports a smaller number of RF transceiver chains than array size. Such architecture intends to solve the power and cost bottleneck of large number of RF-chains. Based on the connectivity between RF-chain and antenna, there are two major variations, fully-connected hybrid array and partially connected hybrid array. Although both architectures were used for Radar application [16] and were introduced for telecommunication application as early as a decade ago [17], they have recently gained much attention for the mmWave radios. Signal processing techniques, including channel estimation and beamforming, using hybrid architecture have been comprehensively studied [18]. Proposals for using hybrid architectures in mmWave 5G

Han Yan and Danijela Cabric are with the Electrical Engineering Department, University of California, Los Angeles, Los Angeles, CA 90024 (e-mail: yhaddint@ucla.edu; danijela@ee.ucla.edu).

Sridhar Ramesh, Timothy Gallagher, and Curtis Ling are with Maxlinear, Inc., Carlsbad, CA 92008.

have been considered in standardization organizations [19].

A handful of works is available on comparative analysis of different mmWave array architectures, with the emphasis on the spectral efficiency [19]–[22]. Some works studied energy efficiency of the array ratio for a particular hybrid architecture. Authors in [23] discussed circuits design challenges in implementation of energy-efficient digital arrays. The relationship between spectral efficiency and energy efficiency in partially-connected hybrid architecture is studied in [24], [25]. Works [15], [20], [26] provided comparison among array architectures and concluded that hybrid architecture can achieve higher energy efficiency than fully digital ones in the regime of point-to-point communication. The future 5G system, however, will unavoidably use multiuser multiplexing as a way to provide higher network throughput. Moreover, existing works did not study trade-offs among array size, transmission power, and specifications of key circuit blocks in the three architectures. However, system designers need to understand these trade-offs and hardware implications to develop energy and cost efficient mmWave systems [27].

This work aims to fulfill this gap. We intend to compare different array architectures in a comprehensive manner by considering trade-offs among capacity, energy and cost efficiency. Specifically, we compare array architectures based on the criterion of achieving same capacity. All design trade-offs are carefully considered in reaching most efficient design in all architectures which meets the requirement of typical 5G use cases. Power consumption, including analog processing energy and digital computation energy, and IC cost are then compared based on the state-of-the-art measurements of circuits components. We provide several design insights on scaling laws and the bottlenecks in each architecture which allow us to predict a trend for future wireless demands and technology scaling.

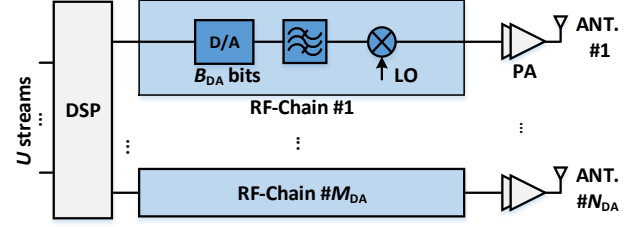
The paper is organized as follows. In Section II, we briefly introduce emerging mmWave array architectures and typical 5G use cases. In Section III, we discuss design trade-offs in all array architectures and the designs used for comparison. In Section IV, we study implementation issues in antenna arrays and their impact on different architectures. In Section V, we present the state-of-the-art specifications of mmWave beamforming circuits blocks and system level power consumption and cost of the three architectures. This leads us to the general conclusions in Section VI.

II. COMPARATIVE FRAMEWORK

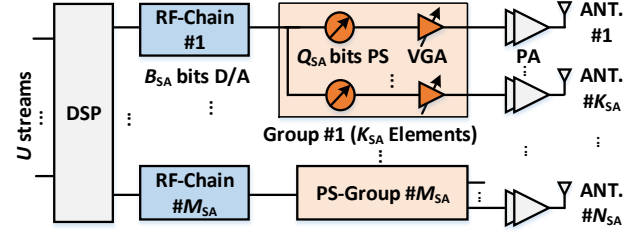
In this work, we focus on the comparison of transmitter antenna array architectures in a 5G mmWave BS. We first introduce three commonly considered array architectures and summarize recent silicon implementations. Then, we describe the metrics used for comparison of the three architectures.

A. Array architectures

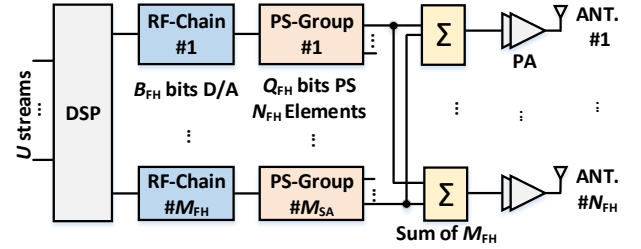
There are three transmitter array architectures that are considered for adoption in 5G system. Regardless of the architecture, the transmission requirements are the same: each array should simultaneously transmits U independent symbol streams and beamform the mmWave signal towards desired



(a) Block diagram of digital array



(b) Block diagram of sub-array. Each RF-chain has the same structure as (a)



(c) Block diagram of fully-connected hybrid array. Each RF-chain and PS group has the same structure as (b)

Fig. 1. Three transmitter array architectures that are considered in this work.

users. In the rest of paper, we treat streams and beams in an equivalent manner.

Fig. 1 depicts block diagrams of digital array and two variations of hybrid array, partially-connected hybrid array (we denote it as sub-array in this work), and fully-connected hybrid array. Key design parameters for each architecture are:

- Transmission power in all array elements: $P^{(out)}$
- Number of antennas: N
- Number of RF-chains: M
- Number of bits in digital-to-analog converter (DAC): B
- Number of bits in phase shifter: Q . This only applies to hybrid arrays.

In the rest of the paper, we use DA, SA and FH when referring to digital array architecture, sub-array and fully-connected hybrid array architecture, respectively. Mathematical symbols with subscript indicate parameters associated with the specific architecture, e.g., N_{DA} represents number of antennas in digital array.

- *Digital Array*: As shown in Fig. 1(a), N_{DA} antennas in DA are connected with M_{DA} RF-chains, i.e., $N_{DA} = M_{DA}$. The number of in-band streams that can be trans-

mitted by digital array U is less or equal to M_{DA} . The beamformer precoding occurs in the digital baseband processor.

- *Sub-Array*: SA consists of multiple phased arrays. As shown in Fig. 1(b), N_{SA} antennas are partitioned into M_{SA} group, each of which has one dedicated RF-chain, K_{SA} phase shifters (PS), variable gain amplifiers/attenuators (VGA), and PAs. The array size, group number, and number of elements in a group follows relationship $N_{SA} = M_{SA}K_{SA}$. Using phase shifters, each group can transmit a beam towards specific direction and SA is capable of transmitting/multiplexing up to M_{SA} simultaneous beams. When the required number of beams U is smaller than M_{SA} , multiple array groups can form a virtual group. The increased array size for that specific beam provides better beamforming performance, e.g., higher gain and narrower beam-width. Digital signal processor (DSP) facilitates precoding multiple beams in the baseband.
- *Fully-Connected Hybrid Array*: This architecture is also known as overlapped sub-array [16], multibeam active phased array [39], and high definition active antennae system [40]. Similar to SA, FH architecture uses phase shifters for analog beamforming and DSP for digital beamforming. However, FH has different connecting structures between RF-chains and phase shifters. As shown in Fig. 1(c), each of M_{FH} RF chains connects with all N_{FH} antennas via phase shifters. Combiner networks are used to add M_{FH} RF signals before passing through the power amplifiers (PA). As a consequence, a total $M_{FH}N_{FH}$ phase shifters are required in this architecture. FH is capable of transmitting up to M_{FH} simultaneous streams.

Recent integrated circuits (IC) implementations of all three architectures are summarized in Table I. Apart from array in 28GHz band, Table. I include implementation in 60GHz band for mmWave indoor access and E-band for mmWave backhaul and radar, because they share the same array architectures. Directly comparing array architectures from the table is difficult. Because they use different silicon technology, and not all circuits components, e.g., local oscillator (LO) and associated up/down-conversion circuits, low noise amplifier (LNA), and power amplifier (PA), are integrated. It is worth noting that SA and FH architectures in Table. I implement phase shifters in the RF domain. Comprehensive survey on phase shifter implementations is covered in [41], including phase shifters in analog baseband, LO, and RF domain. Moreover, system level prototyping of 28GHz arrays together with field test can be found in [19], [42].

There are other architectures that have been recently proposed, e.g., switch based antenna array [43] and lens antenna array [44]. Due to the lack of implementation details available in the literature, we do not include quantitative analysis of them in this work.

B. Comparison metrics under 5G use cases

The 5G is characterized by a wide variety of use cases. They have different environment, communication distance, and

performance requirements, e.g., connectivity density (defined as number of simultaneous connections for one wireless service operator in an given area), peak rate, network traffic throughput. It is our vision that the mmWave BS should be capable of using the same radio front-end arrays to handle various use cases and meet their demands. Three highlighted use cases [45] that we consider in this work are Dense Urban Area, 50+Mbps Everywhere, and Self-Backhauling.

- *Dense Urban*: In the dense urban area, large number of UEs require high-speed connections for applications like streaming, high-definition videos, and downloading files. According to 5G KPI requirement [45], the connection density is expected to be 150,000 connections per square kilometer, while the traffic throughput is up to 3.75Tbps/km² in such scenario. A typical 5G mmWave BS deployment setting has inter-site distance (ISD) to be 200m and each BS has 3 radio sectors [46]. With 850MHz spectrum at 28GHz band, the required spectral efficiency in this use case is up to 58.8bps/Hz. Such scenario often involves line-of-sight (LOS) environment. However, the rate requirement cannot be met without high spatial multiplexing gain. We anticipate that at least 8 simultaneous streams are required.
- *50+Mbps Everywhere*: The electromagnetic wave in mmWave band is extremely vulnerable to blockage. However, BS in the 5G mmWave network should provide baseline performance (up to 100Mbps data rate [45]), for those UEs under unfavorable propagation conditions. The 5G KPI requirement [45] also indicated that the connection density is up to 2,500 connections per square kilometer. With the same BS deployment assumption as discussed in the the previous use case, the required spectral efficiency is 4bps/Hz. It is also anticipated that 2 simultaneous beams are adopted to support connectivity number. Due to the non-LOS (NLOS) environment, severe propagation loss occurs and more than 20dB beamforming gain is expected to close the link budget.
- *Self-Backhauling*: To facilitate ultra-dense mmWave BS deployment, BSs are required to connect to core network through a backhaul link. Since the large array allows interference isolation in the spatial domain, it is expected that 5G BS is capable of using the same spectrum for both access and backhauling, which is refereed as self-backhauling. Self-backhauling using radio for 5G access significantly reduces cost of setting up high-speed fiber. We consider a scenario where mmWave BS transmits uplink data of its local network to a macro-BS receiver which connects to core network. With assumption of one macro-BS deployed in every square kilometer, the self-backhauling link has up to 707m communication distance [47]. In this use case, LOS environment is assumed and 10Gbps rate is targeted.

For fair comparison of power consumption and cost among array architectures we assume that each of them needs to deliver the same required throughput target and the signal to interference plus noise ratio (SINR) in the above 5G use cases, as summarized in Table II. In each use case, the SINR target

TABLE I
SILICON IMPLEMENTATIONS OF MMWAVE ARRAY ARCHITECTURES

Reference, Year	Architecture	Freq. (GHz)	Tx/Rx	Array Size	PA/LNA	LO	Power Consumption per Array Element (mW)	Area per Array Element (mm ²)	Technology
[28], 2017	FH	25-30	Rx	8	-	✓	30 (Rx)	0.77	65nm CMOS
[29], 2017	SA	28	TRx	2	-	-	0 (both Tx and Rx)	1.65	45nm CMOS
[30], 2017	SA	28	TRx	4	✓	-	237.5 (Tx), 142.5 (Rx)	1.23	65nm CMOS
[31], 2017	SA	57-64	Rx	4	-	✓	80 (Rx)	0.65	65nm CMOS
[32], 2016	SA	57-64	TRx	4	✓	✓	167.5 (Tx), 107.8 (Rx)	1.97	28nm CMOS
[33], 2014	SA	57-64	TRx	16	✓	✓	74.4 (Tx), 60 (Rx)	2.07	40nm LP CMOS
[34], 2013	SA	57-64	TRx	32	✓	✓	37.5 (Tx), 26.6 (Rx)	0.89	90nm CMOS
[35], 2017	SA	28	TRx	32	✓	✓	35.9 (Tx), 25.8 (Rx)	5.18	0.13μm SiGe BiCMOS
[36], 2015	SA	57-64	Tx	256	✓	-	10.9 (Tx)	6.79	0.18μm SiGe BiCMOS
[37], 2014	SA	76-85	TRx	8	✓	✓	118.74 (Tx), 143.8 (Rx)	3.26	0.13μm SiGe BiCMOS
[38], 2013	SA	94	TRx	16	✓	✓	181.25 (Tx), 156.25 (Rx)	2.76	0.13μm SiGe BiCMOS

TABLE II
LINK BUDGET ESTIMATION IN TYPICAL 5G USE CASES

Use Case	Dense Urban	50+Mbps Everywhere	Self-Backhauling
Channel Situation	Umi-LOS	Umi-NLOS	Uma-LOS
Freq. (GHz)	28	28	28
BW (MHz)	850	850	850
Distance (m)	100	100	707
Tx Power (dBm)	46.0	46.0	46.0
Tx Antenna Gain (dBi)	3.0	3.0	3.0
Pathloss ^a (dB)	104.4	125.1	118.3
Other Loss ^b (dB)	12.7	25.3	17.0
Rx Gain (dB)	12.0 ^c	12.0 ^c	27.1 ^d
Rx Noise Figure (dB)	10.0	10.0	10.0
Rx Noise Power (dBm)	-74.7	-74.7	-74.7
SNR w/o Tx Array (dB)	18.7	-14.7	15.5
Target Simultaneous Beams	$U = 8$	$U = 2$	$U = 1$
Target SINR w/ Tx Array (dB)	22.1	6.2	35.5

a. Based on 3GPP model for above-6GHz band, [48].

b. Includes shadowing and 25mm/h rain absorption [49].

c. Based on 8 receiver antennas and 3dBi antenna gain.

d. Based on 256 receiver antennas and 3dBi antenna gain.

is set for each stream such that the sum capacity of U streams reaches the throughput requirement. The total transmission power in Table II is 46dBm [46]. For clarity, the design parameter $P^{(out)}$ in Section II-A is normalized, and it denotes the additional transmission power as comparison to 46dBm. The impact of design parameters on SINR performance is presented in the Section III. The power consumption and hardware resources comparison are then presented based on state-of-the-art device specifications.

III. TRANSMITTER ARRAY DESIGN PARAMETERS

In this section, we discuss the impact of array design parameters on the SINR performance of multi-user multi-input multi-output (MU-MIMO) mmWave system. We provide the design specification of components in array architectures to meet the SINR and throughput requirement for each use case.

A. System Model of mmWave MU-MIMO

We consider the mmWave system where a BS transmits to UEs or backhauling destination. Both transmitter and receiver are equipped with antenna array. Linear precoding techniques over flat fading channel are considered. In case of frequency selective channel, the precoding can be extended using orthogonal-frequency-division-multiplexing (OFDM) by considering per sub-carrier precoding. In the baseband equivalent model, the received symbol at the u^{th} UE is denoted as

$$y_u = \mathbf{w}_u^H \mathbf{H}_u \mathbf{R} (\mathbf{B} \mathbf{s} + \mathbf{z}_t) + \mathbf{w}_u^H \mathbf{z}_r. \quad (1)$$

In the above equation, vector $\mathbf{s} = [s_1 \cdots s_U]$ contains the U symbols. Matrix \mathbf{H}_u is the MIMO channel between transmitter and u^{th} UE receiver. Vector \mathbf{w}_u represent the combining beamforming at the u^{th} receiver. \mathbf{B} and \mathbf{R} denote the precoding scheme in the baseband and RF domain on the transmitter side, respectively. The transmission noise due to DAC quantization error is denoted as \mathbf{z}_t and thermal noise at the receiver is \mathbf{z}_r . Operation \mathbf{a}^H is the Hermitian transpose of \mathbf{a} .

In DA architecture, the precoding occurs entirely in digital baseband and therefore there is no analog processing, i.e., $\mathbf{R}_{\text{DA}} = \mathbf{I}$. The digital precoder \mathbf{B}_{DA} has dimension $N_{\text{DA}} \times U$.

In SA architecture, the digital precoder \mathbf{B}_{SA} has dimension $M_{\text{SA}} \times U$ due to M_{SA} RF chains. The RF precoder \mathbf{R}_{SA} has dimension $N_{\text{SA}} \times M_{\text{SA}}$. Due to the fact that every K_{SA} of phase shifters connect to one RF-chain, \mathbf{R}_{SA} is a block diagonal matrix

$$\mathbf{R}_{\text{SA}} = \text{diag}(\mathbf{r}_{\text{SA},1}, \cdots, \mathbf{r}_{\text{SA},M}), \quad (2)$$

where column vector $\mathbf{r}_{\text{SA},m}$ with length K_{SA} represents K_{SA} phase shifters that connect to the m^{th} RF-chain. Each element of $\mathbf{r}_{\text{SA},m}$ has unit magnitude. We define the set $\mathcal{S}_m = \{(m-1)K_{\text{SA}}+1, \cdots, mK_{\text{SA}}\}$ that contains indices of array elements in the m^{th} group.

In FH architecture, the digital precoder \mathbf{B}_{FH} has dimension $M_{\text{FH}} \times U$. The analog precoder matrix \mathbf{R}_{FH} has dimension $N_{\text{FH}} \times M_{\text{FH}}$ and its m^{th} column $\mathbf{r}_{\text{FH},m}$ represents the phase shifting from N_{FH} phase shifters connected to the m^{th} RF-chain, i.e.,

$$\mathbf{R}_{\text{FH}} = [\mathbf{r}_{\text{FH},1} \quad \mathbf{r}_{\text{FH},2} \quad \cdots \quad \mathbf{r}_{\text{FH},M_{\text{FH}}}] . \quad (3)$$

Each element in \mathbf{R}_{FH} has unit magnitude.

We make the following assumptions. Firstly, the channel information \mathbf{H}_u is known to both transmitter and receivers. A practical way of channel estimation can be found in [18]. Secondly, each UE receiver is equipped with a phased array with only one RF-chain. As a consequence, BS assigns one data stream to each UE receiver. Thirdly, all receivers have the same pre-beamforming SNR and BS assigns equal power among data streams. Fourthly, the combining vector of each receiver \mathbf{w}_u is chosen as the primary left eigenvector of channel matrix \mathbf{H}_u after magnitude normalization in each element.

The SINR at the u^{th} receiver array is denoted as

$$\text{SINR}_u = \frac{\|g_u\|^2}{\sigma_{n,\text{rx}}^2 + \sigma_{n,\text{tx}}^2 + \sigma_{\text{int}}^2} \quad (4)$$

where the signal power gain g_u is given by $g_u = \arg \min_g \mathbb{E} \|y_u - g s_u\|^2$. All signal, noise, and interference powers are relative powers, referenced to 46dBm transmit power based on Table II. As a consequence, receiver thermal noise power $\mathbb{E} \|\mathbf{w}_u^H \mathbf{z}_r\|^2 = \sigma_{n,\text{rx}}^2$ is treated as constant in each use case. The multiuser interference is $\sigma_{\text{int}}^2 = \mathbb{E} \|y_u - g_u s_u\|^2$.

In the remaining of the sections, we discuss how to design array parameters for each architecture to reach targeted SINR for three use cases.

B. Array size and transmission power

In principle, increased transmission power $P^{(\text{out})}$ and array size N both improve signal power g_u in (4). Effectively, they provide higher equivalent isometric radiation power (EIRP) and help achieve target SINR from Table II.

In DA and FH, output power of each PA $P^{(\text{out})}/N$ is split into U parts due to multiplexing and even power allocation. Thus each stream in each PA has output power $P^{(\text{out})}/(NU)$. The coherent summation of N -elements via beamforming provides N^2 times increased power. In SA, however, PAs are partitioned into groups to amplify different streams. For each stream, each PA element outputs $P_{\text{SA}}^{(\text{out})}/N_{\text{SA}}$, while the beamforming gain is N_{SA}^2/U^2 . As a consequence, maximum output signal power after beamforming in each architectures is

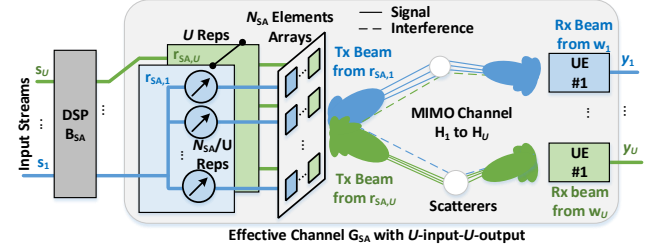
$$G_{\text{DA}} = \frac{P_{\text{DA}}^{(\text{out})} N_{\text{DA}}}{U}, G_{\text{SA}} = \frac{P_{\text{SA}}^{(\text{out})} N_{\text{SA}}}{U^2}, G_{\text{FH}} = \frac{P_{\text{FH}}^{(\text{out})} N_{\text{FH}}}{U}. \quad (5)$$

It is clear that SA is in an disadvantage in terms of signal power gain. SA requires to use more array elements, output power, or both for the comparable output power to DA and FH architectures.

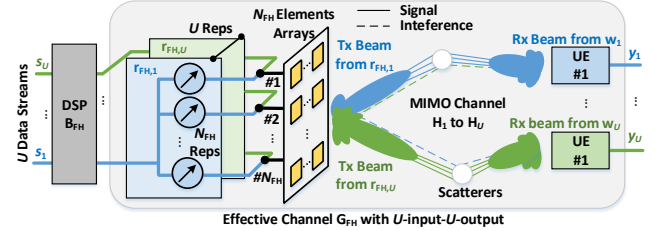
C. Precoder design

Given maximum signal power G , the the precoder determines the actual signal power g_u and multiuser interference σ_{int}^2 in (4). In this subsection, we discuss precoding techniques for three architectures.

In DA architecture, maximum ratio transmission (MRT) and zero-forcing (ZF) are two commonly used linear precoding approaches. The former maximizes the signal strength



(a) In SA architecture, each beam is steered through a group of N_{SA}/U antenna elements.



(b) In FH architecture, each beam is steered through all N_{FH} antenna elements.

Fig. 2. Two-stage precoding in SA and FH architectures. The analog precoder steers spatial beams towards intended receivers. The digital precoder uses regularized zero-forcing over effective channel to handle interference.

at destination and approaches maximum gain discussed in Section II-A, while the latter eliminates multiuser interference. It is commonly believed that because mmWave signals suffer from severe propagation loss, the interference is generally less troublesome than sub-6GHz systems. However, the interference from transmitted sidelobes, if not properly handled, can still affect the achievable rate at receivers. In this work, we propose to use regularized zero-forcing beamforming [50], where the introduced regularization coefficient α_{DA} facilitates controlling both signal strength and interference at the receiver.

$$\mathbf{B}_{\text{DA}} = \kappa_{\text{DA}} \mathbf{G}_{\text{DA}}^H (\mathbf{G}_{\text{DA}} \mathbf{G}_{\text{DA}}^H + \alpha_{\text{DA}} \mathbf{I})^{-1}, \quad (6)$$

In the above equation, \mathbf{G}_{DA} is the post-combining multiuser channel with the u^{th} row as $\{\mathbf{G}_{\text{DA}}\}_u = \mathbf{w}_u^H \mathbf{H}_u$. The regularization coefficient α_{DA} controls the behavior of the precoder, i.e., MRT when it approaches positive infinity and ZF when it approaches zero. One can expect SINR maximization when α_{DA} is selected to be the largest with constraint that $\sigma_{\text{int}}^2 \ll \sigma_{n,\text{rx}}^2$. Power scaling parameter κ_{DA} is used to guarantee total transmission power constraint $\|\mathbf{B}_{\text{SA}}\|^2 = P_{\text{DA}}^{(\text{out})}$.

Precoding approaches with SA and FH architectures are currently actively investigated by researchers. The optimal hybrid precoding is a mixed integer programming problem and its optimal solution must be solved via potentially exhaustive search. Many sub-optimal methods have been proposed for near optimal performance, e.g., works in [51] for FH architecture. In [51], the analog precoder is selected to point beams towards directions of intended receivers. The digital precoder is then used to handle associated interference among beams synthesized by phase shifters.

In SA architecture, we propose to use the following approach as a modification of FH beamforming in [51] and the

scheme is illustrated in Fig. 2(a). We first merge adjacent M_{SA}/U phase shifter groups in SA into one virtual group. It leads to N_{SA}/U array elements within each virtual group in an ideal scenario¹. The input signal of RF-chains within a virtual group are exactly the same. Let us denote set \mathcal{V}_u as one that contains index of physical array groups within the u^{th} virtual group. The analog beamformer is chosen to synthesize beams towards primary propagation direction to U receivers

$$\mathbf{r}_{SA,m} = \exp [j\angle (\{\mathbf{H}_u^H \mathbf{w}_u\}_{\mathcal{S}_m})], m \in \mathcal{V}_u. \quad (7)$$

In the above equation, $\angle(\{\mathbf{a}\}_{\mathcal{S}_m})$ selects elements from vector \mathbf{a} according to indices from set \mathcal{S}_m and finds phases of selected elements. Let us denote the effective channel as \mathbf{G}_{SA} which contains the effect of receiver combiner and RF precoder in multiuser channel. The m^{th} row is defined as $\{\mathbf{G}_{SA}\}_m = \mathbf{w}_m^H \mathbf{H}_m \mathbf{R}_{SA}$. Note the effective channel \mathbf{G}_{SA} is the channel between digitally precoded stream and UEs. As a consequence, the digital precoding problem in SA can be solved in the regularized-ZF framework

$$\mathbf{B}_{SA} = \kappa_{SA} \mathbf{G}_{SA}^H (\mathbf{G}_{SA} \mathbf{G}_{SA}^H + \alpha_{SA} \mathbf{I})^{-1} \quad (8)$$

The power scaling coefficient κ_{SA} is used to meet total output power constraint, i.e., $\|\mathbf{R}_{SA} \mathbf{B}_{SA}\|^2 = P_{SA}^{(\text{out})}$. Similar to precoding in the digital array, the regularization coefficient α_{SA} is chosen to maximize SINR.

The precoding scheme in FH architecture is illustrated in Fig. 2(b). Only U out of M_{FH} RF-chains are turned-on to provides U streams. Without loss of generality, the first U RF-chains are active and the analog precoder is

$$\mathbf{r}_{FH,u} = \exp [j\angle (\mathbf{H}_u^H \mathbf{w}_u)], u \leq U. \quad (9)$$

The digital precoder in FH is a regularized zero-forcing over \mathbf{G}_{FH} , the effective channel that contains the receiver combining and RF precoding in the multiuser channel

$$\mathbf{B}_{FH} = \kappa_{FH} \mathbf{G}_{FH}^H (\mathbf{G}_{FH} \mathbf{G}_{FH}^H + \alpha_{FH} \mathbf{I})^{-1}, \quad (10)$$

The u^{th} row is defined as $\{\mathbf{G}_{FH}\}_u = \mathbf{w}_u^H \mathbf{H}_u \mathbf{R}_{FH}$. Similar to precoding in the SA architecture, κ_{FH} is the power scaling coefficient for $\|\mathbf{R}_{FH} \mathbf{B}_{FH}\|^2 = P_{FH}^{(\text{out})}$ and α_{FH} is the regularization coefficient.

D. DAC precision

The transmission noise in (4) comes from the quantization error due to DACs with finite precision. A practical system design uses sufficient quantization precision such that the transmission noise level stays well below the receiver thermal noise. Different architectures require different values of

effective number of bits (ENOB) for such goal. The required ENOB in three architectures are

$$\begin{aligned} \tilde{B}_{DA} &= \frac{\text{PAPR} - 1.76 + D + 10 \log_{10} \left(\frac{P_{DA}^{(\text{out})}}{\sigma_{n,rx}^2} \right)}{6} \\ \tilde{B}_{SA} &= \frac{\text{PAPR} - 1.76 + D + 10 \log_{10} \left(\frac{P_{SA}^{(\text{out})}}{\sigma_{n,rx}^2} \frac{N_{SA}}{U^2} \right)}{6} \\ \tilde{B}_{FH} &= \frac{\text{PAPR} - 1.76 + D + 10 \log_{10} \left(\frac{P_{FH}^{(\text{out})}}{\sigma_{n,rx}^2} \frac{N_{FH}}{U} \right)}{6} \end{aligned} \quad (11)$$

for transmission noise to be D dB lower than AWGN. In the above equation, PAPR represents the peak to average power ratio of the input signal of each DAC. Note that these expressions are accurate when DAC quantization errors are uncorrelated, which may not be valid with small number of bits, e.g., $B = 1$ bits. Derivations of (11) are provided in the Appendix A.

Equation (11) together with (5) indicates following facts. Firstly, with fixed signal power gain G_{DA} , DACs precision in DA architecture can be reduced by increasing array size and decreasing transmission power. For SA and FH, however, the transmission noise remain constant regardless of the source of signal power gain. Secondly, with the same signal power gain and transmission power, DA architecture has lower requirement in DAC quantization as compared to SA and FH.

E. Phase shifter precision

In both SA and FH architectures, finite resolution of phase shifters leads to a changed power level of sidelobes and shifted location of nulls, as compared to system using ideal devices. More importantly, the locations of main lobe varies and associated signal gain drops. One might expect highly precise phase shifters are required to accurately control beams. In this subsection, we discuss the impact of finite resolution of phase shifters on SA and FH architectures.

The former issue regarding the distorted sidelobes is less troublesome in both SA or FH transmitter array architecture. Sidelobes lead to multi-user interference as seen from the off-diagonal elements in the effective channel \mathbf{G}_{SA} and \mathbf{G}_{FH} . When system is aware of potential interference, digital precoding stage can be used to effectively suppress them. A practical way to acquire the information of effective channel is via a training procedure where BS and UE use quantized analog beamformer to exchange pilot symbols and estimate effective channel \mathbf{G}_{SA} and \mathbf{G}_{FH} . This training procedure is similar to the multi-beam scheme proposed for the next generation of mmWave indoor system [52]. Meanwhile, the gain reduction due to finite phase shifter resolution is not severe either. In fact, the gain degradation is lower bounded by 0.68dB, 0.16dB and 0.04dB with $Q = 3, 4, 5$ bits quantization of phase shifters and does not scale with the array size or multiplexing level. An analysis that supports these numbers is provided in the Appendix B. Equivalently, the gain degradation is bounded by 0.16dB so long as angle error of phase shifters are no larger than 11.25 degree. Such specifications are not difficult

¹Ideal scenario is defined when the ratio M_{SA}/U is an integer. Using a reduced number of arrays can be used when it is not valid, but this scenario is not considered for simplicity.

to meet in state-of-the-art devices as it will be discussed in Section V-C.

F. Simulation results

In this subsection, simulation results are provided to demonstrate the mean SINR performance versus design parameters in three array architectures.

In the simulation, 3D mmWave MIMO channel between BS and U UEs are generated according to mmWave sparse scattering model in [51]. The channel consists of 20 multi-path rays in 1 cluster. Angle of arrival (AOA) and angle of departure (AOD) of clusters are uniform random variables within azimuth range $[-60^\circ, 60^\circ]$ and elevation range $[-30^\circ, 30^\circ]$. AOA and AOD of rays within a cluster have random deviations from the cluster AOA and AOD, and they follow Laplacian distribution. The mean SINR is evaluated by taking average of SINR in (4) over U UEs. The data streams used in the simulation are Gaussian distributed and their magnitudes are truncated such that PAPR is 10dB.

With ideal hardware, the required power to reach SINR target in three architectures are shown in Fig. 3. We make the following observations. Firstly, according to (5), DA and FH architecture have same maximum signal gain when using the same transmission power and number of array elements. In Fig. 3, DA can use around 1dB less transmission power than FH throughout all scenarios. This loss comes from the two-stage precoding scheme of FH. Better hybrid precoding techniques in FH may reduce this gap. Secondly, according to (5), SA architecture requires U times more transmission power than FH when they have the same number of array elements. In Fig. 3, the ratio of required power between SA and FH is close to U in the high- N regime, but larger than U in the low- N regime. With the same array elements, SA steers wider beam than FH since each stream uses a proportion of array elements. In low- N regime, the regularized-ZF in the digital precoder of SA is forced to operate away from MTR to handle interference. As a consequence, more transmission power is required in SA to compensate the loss in precoding. Such phenomenon becomes trivial when the number of antenna elements is sufficiently large. Thirdly, according to (5), double array elements provides 3dB saving in required transmission power in all three architectures. This holds true in Fig. 3, but SA benefits more in low- N regime since narrower beam-width reduces gain sacrificing in precoding. Fourthly, when SA uses U times more elements and same total transmission power as compared to FH, they have the same SINR performance.

With hardware impairment model of DAC and phase shifters, the SINR performance is shown in Fig. 4. For clarity, the output power and array size in each architecture are chosen such that they deliver the same SINR performance in hardware impairment free case. Specifically, both DA and FH architectures use 256 elements and their transmission power is chosen according to Fig. 3. SA architecture uses the same transmission power and U times more array elements as compared to FH. We have the following observations from Fig. 4. Firstly, with the hybrid precoding approach in Section III-C, the SINR performance is negligibly affected by

phase shifter quantization and it matches with our analysis in Section III-E. Secondly, SA and FH essentially have the same SINR performance throughout DAC quantization levels due to the same transmission noise power. Thirdly, the DAC quantization may severely affect SINR performance. According to (11), the required ENOB for transmission noise to be 10dB lower than AWGN in the Dense Urban use case are 4.3, 7.2, and 7.2 in DA, SA, and FH architectures, respectively. The SINR improvement in Fig. 4 is saturated once DAC quantization bits are beyond these values. The DAC precision requirement is relaxed in DA when operating in other use cases as well.

In summary, for the same target SINR performance, DA requires a reduced transmission power or number of array elements as compared to SA and FH. Besides, the DAC quality of DA is relaxed as compared to the hybrid architecture. A fair comparison among architectures cannot overlook these factors by restricting architectures to use the same transmission power, number of array elements, or specification of hardware components. The design parameter trade-off analyzed in this section leads to a more practical comparison in Section VI.

IV. HARDWARE DESIGN CHALLENGES OF TRANSMITTER ARRAY

In this section, we discuss practical hardware design of mmWave arrays with different architectures. We first introduce the distributed array processor module. Then, the necessary circuits blocks for baseband signal and RF signals distribution are discussed.

A. Distributed array module

The conventional MIMO system integrates array processing module in an IC and delivers RF signal to antennas. Such centralized design may not be practical in mmWave system with massive number of antennas. With a compact and centralized IC, mmWave signals routed to hundreds of array elements suffer severe insertion loss². Besides, the heat dissipation becomes a concerns for a centralized solution. Moreover, array size scalability becomes challenging since adding more elements requires completely new processing module.

A practical solution is to implemented processing hardware of antenna arrays in a distributed manner [23]. In DA and SA, each IC in a processing module integrates the processing circuits for K_{DA} and K_{SA} antennas and is located close to these antennas. Although a centralized digital processor may still be necessary for baseband processing, including symbol mapping and channel coding, RF components and PAs are included in the processing module. The digital signals from central processor are routed and recovered through Serializer/Deserializer (SerDes) sub-system in each of the processing modules. Note that the exact value of elements integrated in an IC affects system cost and energy. But the discussion of that is beyond the scope of this work. Each of the array modules also contains substrate for antenna integration, such as low temperature co-fired ceramics (LTCC) [53], multi-layer organics (MLO) [54].

²The wavelength at 28GHz band is 10.7mm, 256 antennas in a square alignment with half-wavelength require at least 7327mm².

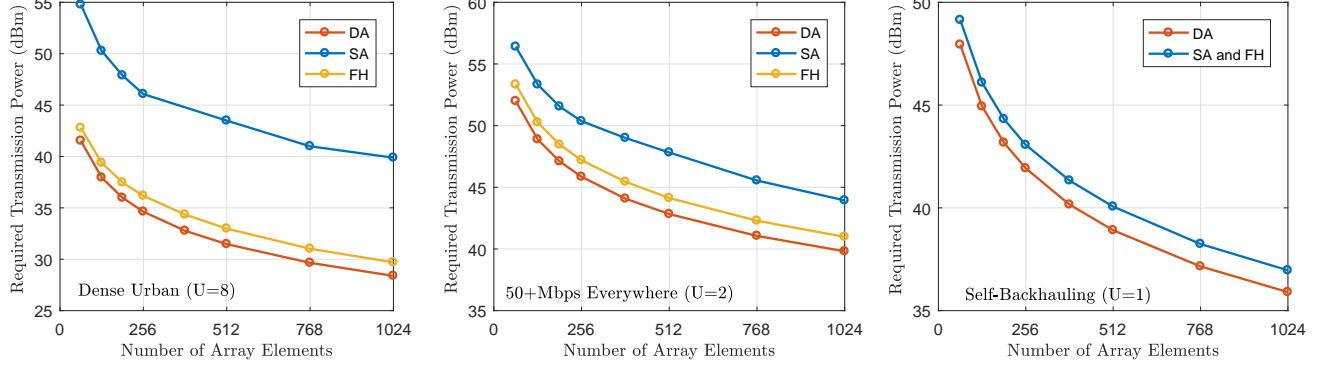


Fig. 3. The required total transmission power $P^{(out)}$ with different number of array elements (N) to reach SINR target in three typical 5G use cases.

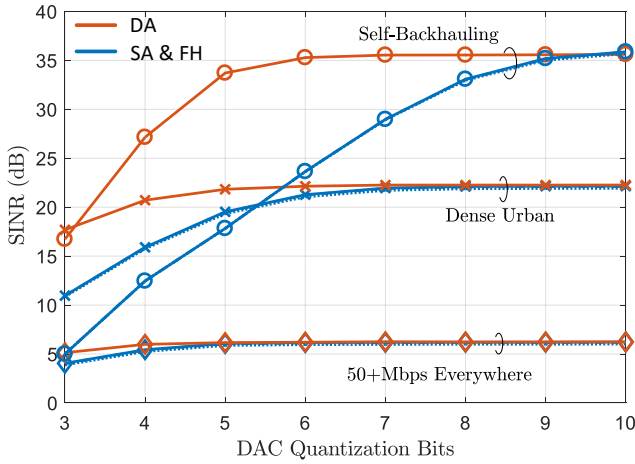


Fig. 4. SINR performance with different hardware impairments. Three architectures use $\{N_{DA}, N_{SA}, N_{FH}\} = \{256, 2048, 256\}$ array elements and output power is scaled for the same throughput performance assuming ideal hardware. SA and FH architectures equipped with $Q = 3, 4, 5$ bits phase shifter are shown in dotted, dashed, and solid curves, respectively. The baseband precoding uses fixed point operation with precision 2 bits greater than associated DAC quantization which ensures negligible degradation as compared to baseband precoding with floating point operation.

The illustration of distributed DA hardware implementation is shown in Fig. 5(a). In the remaining of the paper, power consumption and cost estimation of DA system is based on design where each module contains $K_{DA} = 8$ antenna elements and associated processing circuits. Each DA module contains SerDes, voltage controlled oscillator (VCO) within a phase-lock-loop (PLL), and RF-chains and T/Rx multiplexers. The power amplifiers for 5G mmWave applications are expected to be built in non-silicon material, as shown in Section V-D and they are placed next of DA processing IC.

The illustration of SA implementation is illustrated in Fig. 5(b). In SA, each module has processing circuits for $K_{SA} = 16$ antenna elements. Each of them contains SerDes, VCO and phase shifter networks.

There is no priori work of FH implementation with larger than 8 antennas. The RF signal routing is a challenging task

in FH architecture, because the input signal for each antenna element is a combination of signals from all RF-chains. The most viable approach we could anticipate is illustrated in Fig. 5 (c). As the opposite of DA and SA architectures, routing loss cannot be reduced by distributing RF-chains into a closer position, since their outputs are required to be delivered to entire PCB board. In the proposed design, each array module integrates a combining network and delivers the combined signal to nearby antenna elements. It also contains RF amplifiers to compensate for insertion loss during the RF signal routing and combining.

In all array architectures, routing digital baseband signal and RF signals plays a critical roles. We discuss associated challenge and solutions in the next subsections.

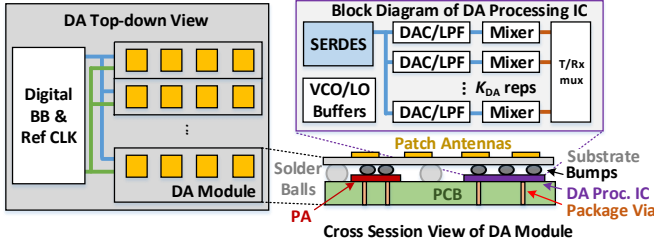
B. BB signal distribution

The digitally precoded sample streams require to be routed into each processing module by serial-link transceivers in all array architectures. The state-of-the-art SerDes supports data rates over 50Gb/s using PAM-4 signaling in wireline chip-to-chip communication. The specific design of SerDes system is beyond the scope of this work. In Section V, we use the specifications of ultra-high-speed transceivers.

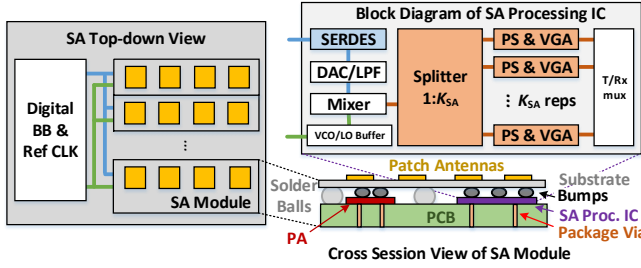
C. RF signal distribution

Multiple circuit components introduce non-negligible insertion losses that need to be carefully handled by system designers.

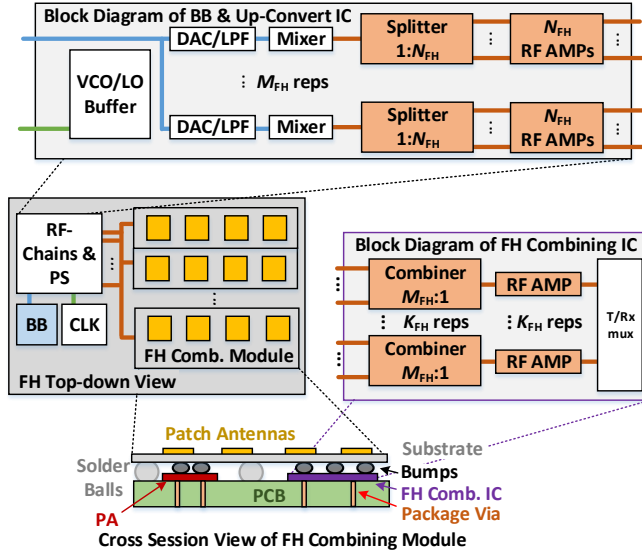
- *PCB and Inter-Connectors Loss:* RF signal suffers from interconnect loss between the silicon chip RF ports and the antenna elements. The low-loss PCB board, such as RO 3000 series and 4000 series, 28GHz signal have 1.25dB/inch insertion. Besides, each IC chips require to be placed on organic or ceramic substrate (interposer) to distribute the chip ports to a ball-grid array and it has an additional 1-2dB distribution loss. This implementation loss needs to be properly compensated before signal is fed into antenna.
- *Intra-Chip Transmission Lines Losses:* RF signal loss in silicon is significant at mmWave band. According to [36], there is up to 0.6dB/mm transmission line loss at 28GHz.



(a) System module diagram of digital array



(b) System module diagram of sub-array



(c) System module diagram of fully-connected hybrid array architecture.

Fig. 5. The board plan in top-down view and cross section view, and RFIC components of three array architectures. Blue, green, and red line represents for baseband, reference clock/LO, and RF signal routing.

The length of transmission line is proportional to the IC size but exact value is determined by actual IC design. According to a 60GHz array design [55], phase shifter and Wilkinson RF splitter takes most of the IC area. The intra-chip routing loss can be roughly estimated by taking account the required area of those components. With the practical components size in Section V, the loss in an SA module with $K_{SA} = 32$ phase shifters is less than 1dB but up to 3-4dB for FH since each RF-chain distributes signals into hundreds of phase shifters which requires

dozens of millimeter square area.

- *Power Splitters and Combiners Loss:* In the analog beamforming stage of SA and FH architectures, output signals of RF-chains need to be fed into phase shifter network for phase rotation. The Wilkinson power splitters are commonly used for such purpose [28], [29], [55]. Moreover, the fully-connected hybrid architecture uses same Wilkinson structure to combine multiple RF signals before power amplification. An ideal power splitter/combiner introduces 3dB insertion loss in each of the one-to-two splitter (1:2) or two-to-one combiner (2:1) unit. Practical design often has an additional 1dB implementation loss. It results in a $4 \log_2(K_{SA})$ dB power drop in the SA architecture. For FH architecture, the splitters and combiners introduce total $4 \log_2(N_{FH}M_{FH})$ dB loss.

All the above RF insertion losses lead to an reduced EIRP at the antenna and therefore need to be properly compensated. The detailed distribution budget in all architectures is discussed in Section. V-D.

V. HARDWARE POWER AND COST MODELING

In this section, we first provide the power and cost model of necessary circuits blocks based on a survey of the state-of-the-art circuits design and measurement. The power consumption contains DSP module for precoding, SerDes, mixed signal components, and RF components. Note that other hardware blocks such as power supply, active cooling may consume considerable power [56]. We omit them in this work since these are constant hardware overhead. Then, examples are provided for signal distribution budgets calculation in order to determine necessary RF amplifiers to compensate insertion loss. Finally, we summarize the total power and cost calculating formula for all architectures operating with different design parameters.

A. Digital signal processing power

Due to large bandwidth, the array processing in the digital baseband needs to support such high throughput. The DSP for array processing mainly consumes power for digital precoding and digital signal routing. Note that tasks such as channel coding, higher layer processing in the communication standard stack are not included since they have equal power consumption for all architectures. Channel estimation and precoder computation are also omitted since they occur at time scale that is several orders of magnitude longer than symbol duration.

The DSP power estimation contains linear precoding and 4096 point inverse discrete Fourier transform³ (FFT). The precoding requires multiplication of $M \times U$ complex matrix with $U \times 1$ complex vector. It has $6UM$ fixed points operations. Note that the number of operation does not change with different design choices of N_{FFT} , because the number of precoder slices in sub-carriers and symbol duration change. The latter consists of $\log_2(N_{FFT}) = 12$ complex multiplication per sample per RF-chain, and it results in $6 \times 12M \times BW$ operations per second. We use $FOM_{DSP} = 13GOPS/mW$ in

³We assume $N_{FFT} = 4096$ point IDFT for 850MHz signal bandwidth to achieve 3GPP-specified subcarrier spacing 240KHz [57]

40nm CMOS as state-of-the-art fixed point digital computation efficiency [58]. As a consequence, the power consumption in the digital precoding is

$$P_{\text{Precoding}} = \frac{(6UM + 72M) \times \text{BW}}{\text{FOM}_{\text{DSP}}} \quad (12)$$

where BW is the signal bandwidth. The power consumption $P_{\text{Precoding}}$ has unit Watt.

The power of SerDes system is modeled in the following equation

$$P_{\text{SerDes}} = \text{FOM}_{\text{SerDes}} \times \text{BW}_{\text{OS}} \times \text{ENOB} \times M \quad (13)$$

In the above, ENOB is the required precision in the DAC of mmWave transceiver and its value determined according to the analysis in (11). The figure-of-merit of SerDes is adopted as $\text{FOM}_{\text{SerDes}} = 10\text{mW}/(\text{Gb/s})$ [59] in this work. Note here we use BW_{OS} as the oversampled data rate after considering a factor of 2 oversampling ratio, i.e., $\text{BW}_{\text{OS}} = 1.7\text{GS/s}$.

B. Power model of mixed signal components

In section III-D, we analyze the impact of DAC quantization in different array architecture. The DAC power consumption is mainly determined by the sampling frequency and effective number of bits. The total power consumption in each DAC is computed using the following equation

$$P_{\text{DAC}} = \text{FOM}_{\text{DAC}} \times (2^{\text{ENOB}} \times \text{BW}_{\text{OS}}) \quad (14)$$

where P_{DAC} has unit. BW_{OS} and are similarly define in (13). The state-of-the-art specification of DAC is $\text{FOM}_{\text{DAC}} = 0.08\text{PJ}/\text{conversion}$ [60].

C. Power model of RF signal components

In this section, we estimates the required power consumption in the RFIC, including the power for signal amplification and analog array processing for hybrid architecture. The components are phase shifter, local-oscillator using phase-lock-loop (PLL), mixer, RF amplifier for gain compensation, and the power amplifier for transmission.

- *Local oscillator (LO) and mixer:* The phase noise of an oscillator is inversely proportional to the power dissipated [23]. The state-of-the-art VCO design [61]–[64] facilitates lower than $-110\text{dBc}/\text{Hz}$ at 1MHz by using less than 30mW DC power consumption. Minor rate reduction occurs with such phase noise level [65]. Considering the required buffer at the output, the power consumption of VCO block can be $P_{\text{VCO}} = 60\text{mW}$ for each element. Mixer can be made by active or passive devices. Practically, passive mixers are easier to implement and performance with better linearity and noise. Mixers requires enough LO signal power to be driven. In this work, we selects the inputs LO power to be at least -5dBm and the power consumption of mixer is $P_{\text{Mixer}} = 10\text{mW}$. The total power consumption in LO is $P_{\text{LO}} = 70\text{mW}$
- *Phase shifter:* RF phase shifting can be implemented in various ways, see [41] for a comprehensive survey. The state-of-the-art work uses reflective-type phase

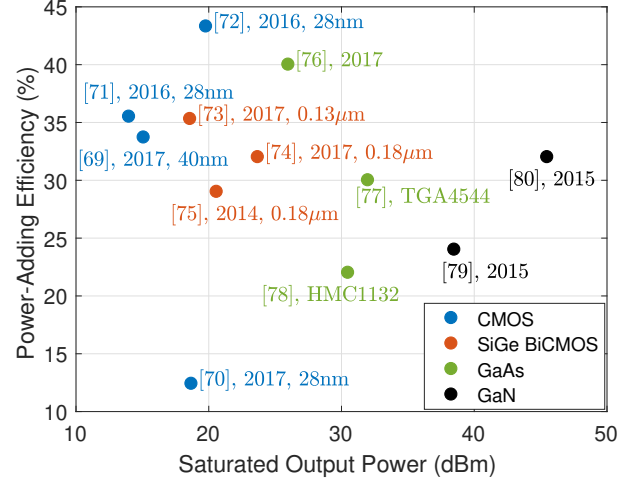


Fig. 6. The saturated output power and power-added efficiency at that power level (PAE_{max}) of the state-of-the-art power amplifiers at 28GHz . Data are from [70]–[81] and labels include publication date and silicon technology.

shifter (RTPS) and switch-type phase shifter (STPS) as main approach of passive PS [29], [30], [66]–[68]. Such approaches use delay line with controllable length to generate desired phase shifting. Although nearly zero DC power consumption is required, passive PS often evolves with high insertion loss and large IC area due to the delay line. The active approach uses vector modulator (VM), which consists of variable gain amplifier in both In-Phase and Quadratic RF path to generate a complex gain as phase shifting coefficient. VM requires active devices and have higher power consumption than STPS or RTPS. Meanwhile, VM requires less IC area [28], [55], [69]. In this work, we use VM for building block of hybrid architecture and the power model is $P_{\text{PS}} = 10\text{mW}$ with 2dB gain.

D. RF signal amplification power

The RF signals amplification has two category: gain compensation amplifier and power amplifier.

- *RF amplifier:* Gain compensation amplifiers are used to compensate insertion loss in the analog beamforming for hybrid architectures. As discussed in Section IV, hybrid architectures require to distribute up-converted RF signal into phase shifter networks. During this procedure, insertion loss is introduced in power splitter, transmission line and power combiner. These losses need to be properly compensated in order to deliver sufficient radiated signal power at the antenna. From the cost perspective, it is better to provide the gain before power splitting occurs since it requires fewer number of amplifiers. However, it raises the linearity concern of CMOS amplifier. As it is shown in the next subsection, a large hybrid array has more than 20dB insertion loss in the distribution route and in order to pre-compensate such loss immediately after up-conversion leads to a severe nonlinear distortion in RF signals. Practical design typically place amplifiers

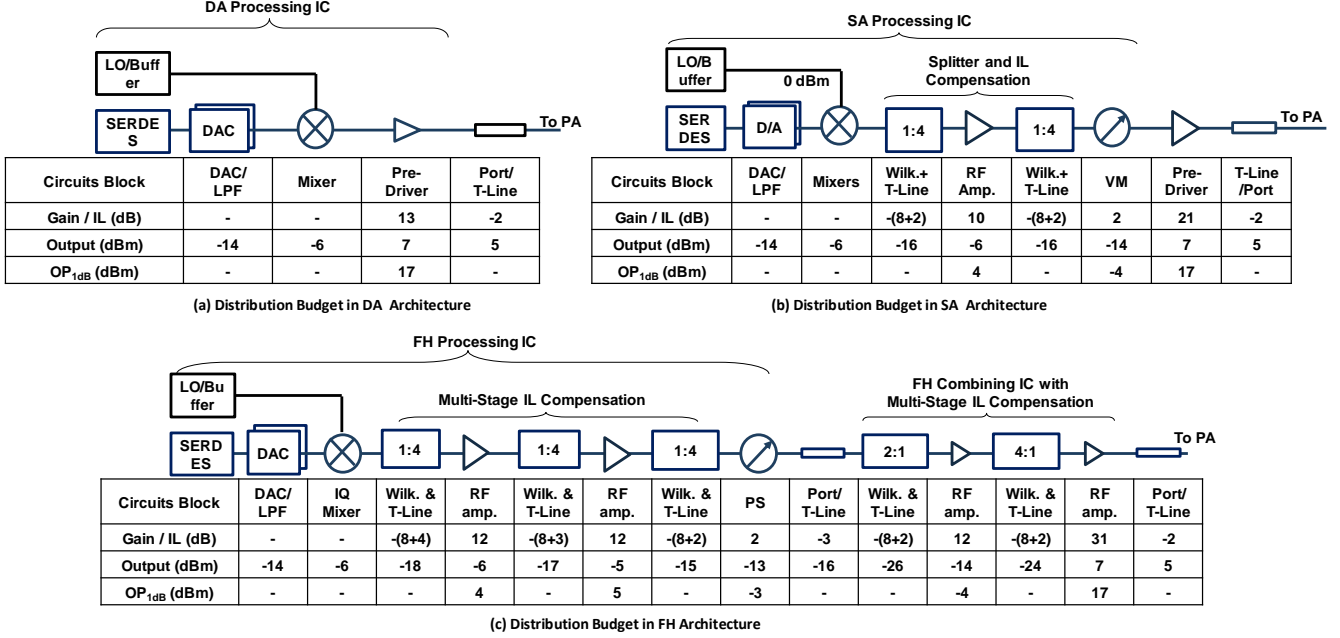


Fig. 7. The signal distribution budget example of three array architectures.

in a hierarchy manner along RF signal distribution route [55]. Besides, the gain compensation amplifiers need to be carefully designed and their power consumption cannot be overlooked. The power model adopted in this work considers gain compensation amplifier design from [36], where each amplifier has up to 15dB gain with $P_{\text{Amp}} = 40\text{mW}$ power consumption. Note that active combining [28] is an alternative approach that combines RF signal in current mode using low-noise amplifiers. Although insertion loss can be avoided, there is power consumption in each combiner. We do not discuss this approach in details.

- **Power amplifier (PA):** Power amplifiers take large amount of power in current base-stations operating in sub-6GHz band. In the mmWave BS system design there are two conflicting scaling direction. On one hand, the emitting power of each PA is relaxed due to the use of massive antenna array for similar total power. On the other hand, the power amplifier efficiency is lower than those designed for sub-6GHz band. In Fig. 6, specifications of the state-of-the-art mmWave power amplifier at 28GHz are shown. Specifically, the power-added-efficiency (PAE) at saturated output power and associated saturated output power are presented. Different semiconductor technologies, e.g., CMOS, BiCMOS, Gallium Arsenide (GaAs), and Gallium Nitride (GaN) are included. The state-of-the-art CMOS or SiGe BiCMOS PAs are not suitable due to the low saturated output power. Assuming 10dB PAPR margin, even with an extremely large array of 1024 elements, the 46dBm total transmitter power leads to 16 dBm output power for each element. Thus 26dBm headroom of PA is expected and it can be barely reached

by interpretable PAs. GaAs PAs are generally cheaper than GaN PAs and are expected for 5G array applications without operating in strongly nonlinear region. In the proposed PA power consumption model, a PA efficiency is $\eta_{\text{PA}} = 0.185$ is adopted. Specifically, the calculation of PA efficiency is based on 0.3 peak PAE, 10dB power back-off, and a Doherty PA architecture⁴. Accordingly, the power consumption in each PA element is

$$P_{\text{PA}} = \frac{P^{(\text{out})}}{N\eta_{\text{PA}}}, \quad (15)$$

where the number of array elements N and output power $P^{(\text{out})}$ are from Fig. 3 in each architecture.

E. Summary of specifications of circuits blocks for transmitter array architectures

In Fig. 7, we present the signal distribution budget example of three array architectures with 64 elements. Specifically, we focus on the insertion loss in PCB, silicon, and RF devices as modeled as in Section IV. There is more than 10dB loss for every two stages of Wilkinson splitters/combiners plus associated transmission line. As a consequence, RF amplifiers can be placed to compensate such loss in SA as shown in Fig. 7(b). For FH, multi-stage compensation is required to avoid saturation as shown in Fig. 7(c). Such design is

⁴In Doherty PA, the PAE remain constant when the instantaneous output magnitude a is no more than 3dB weaker than the peak magnitude a_{max} , i.e., $\text{PAE}(a) = \text{PAE}_{\text{max}}, a \geq a_{\text{max}}/2$. Otherwise, the PAE drops as a linear function of instantaneous output magnitude, i.e., $\text{PAE}(a) = \frac{2a}{a_{\text{max}}} \text{PAE}_{\text{max}}, a < a_{\text{max}}/2$. Thus, the average efficiency is $\eta_{\text{PA}} = \int_a f_A(a) \text{PAE}(a) da$, where $f_A(a)$ is the probability distribution of signal magnitude. When $\text{PAE}_{\text{max}} = 0.3$ and the signal magnitude is Rayleigh distributed with average power 10dB below the peak, PA efficiency is $\eta_{\text{PA}} = 0.185$.

commonly adopted in implementation of phased array [55]. Moreover, a combining network in FH also needs similar design. For a splitting or combining network with N_{wilk} ports, we use an approximation number of $\sum_{n=1}^{\infty} N_{\text{wilk}}/4^n \approx N_{\text{wilk}}/3$ amplifiers for simplicity. As a consequence, FH requires a total $UN_{\text{FH}}/3$ amplifiers in both splitting and combining network. Moreover, for all architectures, we assume a 5dBm signal strength is required at the input of PA [78], [79]. The output of each mixer is -6dBm. For a Wilkinson splitter or combiner with N_{wilk} ports, a total $N_{\text{wilk}} - 1$ 1:2 or 2:1 units are required. As a consequence, the required number of Wilkinson units are $(K_{\text{SA}} - 1)N_{\text{SA}}/K_{\text{SA}}$ and $U(N_{\text{FH}} - 1) + N_{\text{FH}}(U - 1)$ in the SA and FH architectures, respectively. A summary of specifications of circuits blocks, total number of blocks in each architectures, and required number of blocks per antenna element are summarized in Table. III.

VI. COMPARISON RESULTS

In this section, we present the power and hardware cost comparison among three architectures. Then, we discuss the scalability of these architectures for future trends. Specifically, we focus on the impact of increased throughput requirement and improved energy efficiency in digital computation due to silicon scaling.

A. Power and IC area of mmWave array architectures

The required power consumption in transmitter array systems when delivering target rate requirement in Dense Urban use case is shown in Figure 8. We draw the following observations. Firstly, in designing the 5G mmWave transmitter array, one can reduce the power consumption of PAs without losing performance. This benefit comes from using beamforming with larger array size to reduce the total transmission power. Since the power consumption of PAs is the bottleneck of most current BSs, total system power can be reduced by using large antenna arrays. However, increasing array size requires additional processing power. In Figure 8, all three architectures have green points in terms of array size that minimizes system power consumption. At the green point, a balance is reached between PA power and processing power in other circuits blocks. Secondly, DA and FH have the same green point with $N_{\text{DA}} = N_{\text{FH}} = 128$ array elements. For larger array size, the processing power in the wireline data link and LO are the limiting factor for DA. Although existing works are skeptical about digital array architectures due to potentially excessive power in DSP and data converters [15], our results show that they are less critical due to favorable figures-of-merits of current IC design and the word-length reduction provided by transmission array. The power in IL compensating amplifiers becomes limiting factor of processing power in FH which is N times higher than green point. Thirdly, due to the disadvantage of using array gain (5), SA essentially needs to use U times more antenna array elements as compared to DA to have similar power consumption in PAs. Accordingly, the green point for SA is at $N_{\text{SA}} = 768$ antenna elements. Since the processing power per array element in SA is significantly low (73mW in SA v.s. $\sim 200\text{mW}$ in DA), SA can afford

to use higher number of elements and reach similar power consumption to DA and FH. In summary, with optimized array size, DA architecture has advantage by using 52% and 35% less power than SA and FH architecture, respectively.

The power consumption in the other two use cases are shown in Figure 9. In this figure, the green point for array size is chosen for each architecture and thus they reach balance between transmission power and processing power. The hybrid array architectures (SA and FH) have advantages in these two use cases. Due to the smaller number of required beams, gain dropping in (5) for SA is much smaller than in dense urban scenario. Therefore SA can use array size similar to DA for similar PA power consumption and the benefits of lower per-element processing power results in a lower system-level power than DA. FH also has benefit due to small number of required simultaneous beams U because the number of IL compensation amplifiers linearly depends on U which is the power bottleneck of FH. In summary, in use cases where small number of beams are required, both SA and FH are more efficient from total power consumption perspective.

However, the hardware cost of operating at green point of array size is different in three architectures. In Figure 10, the required IC area is presented as function of array size. Note that all architecture requires hardware to support $U = 8$ beams. For DA architecture at green point $N_{\text{DA}} = 384$ uses 172mm^2 area while SA with $N_{\text{SA}} = 1024$ requires 248mm^2 . FH architecture uses far more hardware resources due to large number of phase shifters and Wilkinson units to support full-connection between RF-chain and antenna arrays.

B. Comparison of Scalability for Future Demands

From the result above, SA architecture is shown to be a suitable architecture for current 5G requirement. Actually, many 5G mmWave system prototypes are implemented based on such architecture. However, greater challenge arises with the increased future demands.

According to [83], the mobile data requirement increases at a compound annual growth rate of 42%, and this trend will likely remain in the era beyond 5G. The scalability of 5G mmWave BS for future demands is an important factor in comparison among array architectures. Adapting existing BS to support higher multiplexing level is an effective way to support the increased throughput requirement and it is more cost effective than planing additional spectrum or deploying BSs in a more dense manner. Meanwhile, more advanced silicon techniques and digital signal processing enable cheaper and more energy efficient implementation. In Figure 11, the power consumption of DA and SA with increased throughput demands and DSP FOM are depicted in a dense urban use case. In this figure, the power consumption is based on optimized array size. We have the following observations. Firstly, DA architecture requires a small proportion of increased array size and total power consumption of the system. Actually, DA architectures only requires to activate the idle arrays in a 384-element design suitable for current use cases. Secondly, SA architecture requires larger increment in both hardware and power consumption. Note that the total power consumption

TABLE III
SUMMARY OF CIRCUITS BLOCKS IN ARRAY ARCHITECTURES

	BB DSP	SerDes ^h	DAC	LO/Mixer	PS	Splitter/Combiner ^b	RF Amp. (IL Comp.)	RF Amp. (Pre-Driver)	PA
DC Power per Block	eq.(12)	eq.(13)	eq.(14)	60+10mW	10mW	-	40mW	40mW	eq.(15)
IC Area per Block (mm ²)	-	1.21 ^c	0.05 ^d	0.18 ^e	0.05 ^f	0.04 ^g	0.025 ^f	0.025 ^f	-
Blocks in DA ^a	1	N_{DA}/K_{DA}	N_{DA}	-	N_{DA}	-	-	N_{DA}	N_{DA}
Blocks in SA ^a	1	N_{SA}/K_{SA}	N_{SA}/K_{SA}	N_{SA}	N_{SA}	$N_{SA} - N_{SA}/K_{SA}$	$N_{SA}/4$	N_{SA}	N_{SA}
Blocks in FH	1	-	U	UN_{FH}	UN_{FH}	$2N_{FH}U - N_{FH} - U$	$2UN_{FH}/3$	N_{FH}	N_{FH}
Blocks per DA Antenna	N/A	$1/N_{DA}$	1	-	1	-	-	1	1
Blocks per SA ^a Antenna	N/A	$1/K_{SA}$	$1/K_{SA}$	1	$1 - 1/K_{SA}$	1/4	1	1	1
Blocks per FH Antenna	N/A	-	U/N_{FH}	U	$2U - 1 - U/N_{FH}$	$2U/3$	1	1	1

a. We do not focus on varying the number of elements in module. $K_{DA} = 8$ and $K_{SA} = 16$ are treated as constants.

b. It refers to a 1:2 or 2:1 Wilkinson splitting or combining unit.

c. We use 0.89mm² [59] and 0.32mm² [82] for SerDes receiver and transmitter respectively. They are fabricated in 28nm and 16nm CMOS.

d. Specification is from [60] and the DAC has 8 bits precision and uses 28nm fabrication.

e. Specification of 28GHz LO and mixer are from [63] and 65nm CMOS fabrication is used.

f. Specification is estimated from figure in [55]. 0.18μm BiCMOS is used for fabrication.

g. Specification is estimated from figure in [55] and scaled by wave-length due to its direct impact in Wilkison divider.

h. Assuming SerDes module is used for each module define in Section. IV-A.

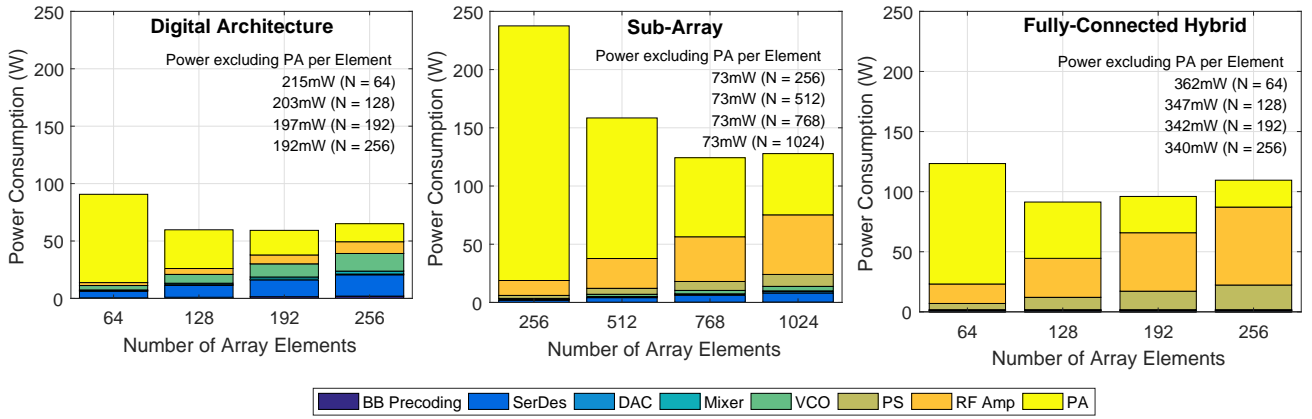


Fig. 8. Total power consumption for three architectures operating in the Dense Urban use case. For each array architecture with varying array size, other design parameters are chosen according the analysis in Section III and throughput demands are guaranteed. Processing power (excluding non-silicon PA) per array element are listed in text.

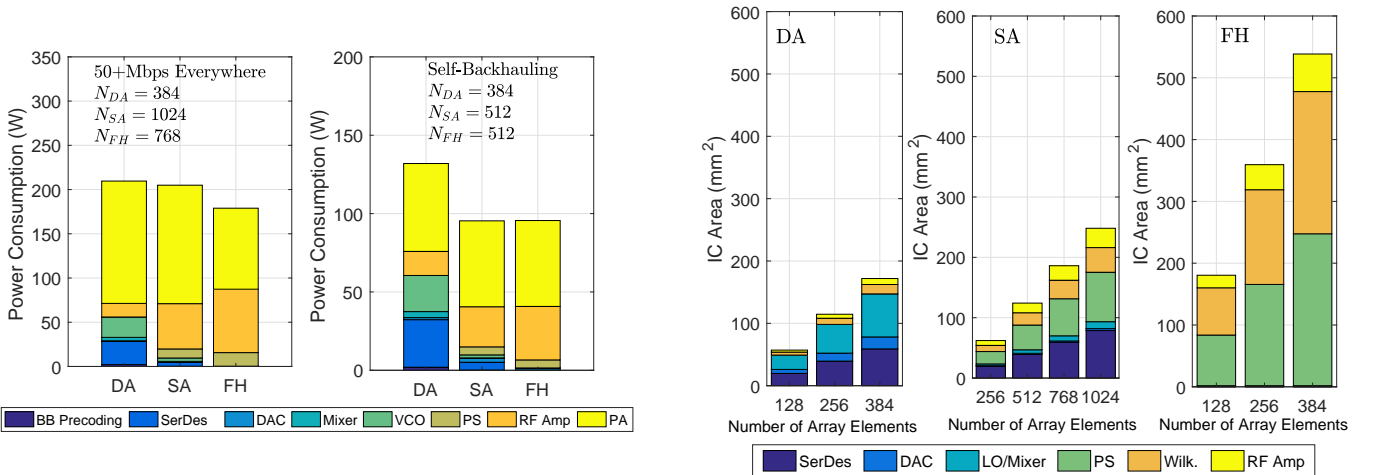


Fig. 9. Total power consumption for three architectures when the throughput requirements in use cases are met. Each architecture uses array size that reaches lowest power consumption.

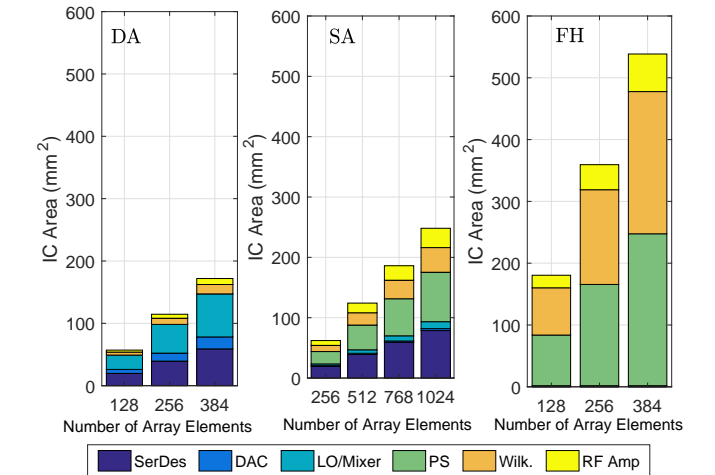


Fig. 10. IC area breakdown of three architectures. Each of architecture uses array size such that it can meet 5G use cases throughput requirement in an energy efficient manner.

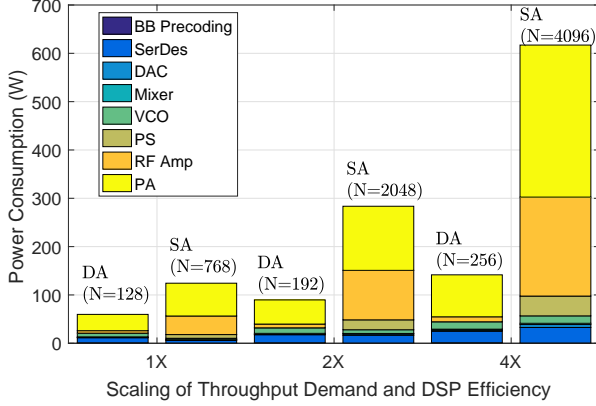


Fig. 11. The required power consumption in DA and SA architecture when both are designed to meet the demands of the increased network throughput. DSP efficiency improvement in the future is also included.

in SA is much larger than the value in the figure if one uses $N_{SA} = 1024$ elements to meet the increased throughput by increasing transmission power. Although additional hardware cost is expected for SA for scaled throughput demands, the IC design of SA module remains the same and it makes it a viable option. In FH architecture, however, changing the number of RF-chain requires redesigning the hardware of combining IC.

VII. DISCUSSIONS ON OPEN RESEARCH CHALLENGES

Admittedly, the power and IC area analysis for three array architectures provided are mere speculation. In particular, the effect of the extra digital processing on power consumption and area depends on actual design and are hard to analyze at this point. Besides, some open research questions remain and were not covered in this paper. First one is the issues of synchronization among large array elements. In the centralized LO distribution architecture, each element re-generates clock from the same references but global LO distributing may not be area and energy efficient [84]. Under distributed LO scheme, independent LOs help reduce impact of phase noise [85] but system needs to be calibrated periodically to avoid loss of coherency across elements. Second issue is related to compensation of PA nonlinearity. Digital predistortion (DPD) is important in massive transmitter array design. Conventionally, DPD is designed and implemented for each transmitter chain independently. Due to increase processing and power of DPD, the overall gains in power efficiency for large number antenna arrays need to be analyzed and optimized.

In this work, we reveal that the conventional belief that hybrid array architecture is more cost and energy efficient than digital architecture is not necessarily true when comprehensive hardware design is modeled and optimized. Similar findings were reported for the receiver array during the period when this work is written [86], [87]. It is worth noting these works including ours focus on the linear MIMO processing model and the additive uniformly distributed quantization error model. However, linear MIMO processing is not optimal and quantization error model is not valid when data converters have significantly small number of bits. In fact, in the receiver array

a variety of nonlinear combining and decoding algorithms are proposed, e.g., successive interference cancellation based combining [25], approximate message passing [88]. Besides, the precision requirement of DAC and analog-to-digital (ADC) devices are strongly dependent on processing algorithms, e.g., algorithm tailored for 1-bit ADC [89]. It remains open research questions to use advanced signal processing to further reduce power consumption and cost of mmWave array.

VIII. CONCLUSION

Building energy and cost efficient massive array is one of the major challenge in implementing and deploying mmWave networks in the 5G era. In this work, we study and compare three array architecture candidates, digital architecture and two variation of analog-digital hybrid architectures and discuss various hardware design trade-offs. Specifically, the required power and hardware specifications of key circuits blocks are modeled as function of array size in each architecture. Based on the state-of-the-art circuits design and measurement results, we evaluate the power and cost of circuits blocks in each architecture and identify the optimal array size of each architecture. The results show that both digital architecture and partially-connected hybrid architecture are suitable for current 5G use cases although digital architecture is a cheaper option. Moreover, digital architecture shows better scalability with increased throughput requirements and improved energy efficiency of DSP.

IX. ACKNOWLEDGMENT

The financial support of National Science Foundation through grant 1718742 is gratefully acknowledged.

APPENDIX

A. Required DAC quantization bits

In this subsection, we provide analysis of transmission noise $\sigma_{n,tx}^2$ in each architecture.

For each DAC, the quantization error is uniformly distributed in $[-A/2^B, A/2^B]$ where A is the largest quantization level. Without signal cropping, A depends on the peak-to-average-power-ratio (PAPR), i.e., $PAPR = A^2$ with unit signal power. The power of DAC quantization noise is

$$\epsilon_{DAC}(B) = 10 \log_{10} \left[\frac{(2A)^2}{12(2^B)^2} \right] = 10 \log_{10}(A^2/3) - 6B \text{ [dB]}. \quad (16)$$

Note that the above power is normalized with the input signal power of each DAC.

In DA architecture, the input signal power of DAC is amplified to $P_{DA}^{(out)}/N_{DA}$. As a consequence, the transmitter noise power at output of each PA is $P_{DA}^{(out)} \epsilon_{DAC}(B_{DA})/N_{SA}$. With the uncorrelated⁵ quantization errors in each DAC, transmission noise is $\sigma_{n,tx}^2 = P_{DA}^{(out)} \epsilon_{DAC}(B_{DA})$.

⁵Correlation among quantization errors of DACs become non-negligible when quantization level is significantly small, e.g., one bit. Dithering is a technique to de-correlate them but is beyond the scope of this work.

In SA architecture, due to the identical input signal of DACs in a virtual group, quantization noise remains the same as well. The quantization noises are coherent at the outputs of N_{SA}/U PAs within a virtual group and each has power $P_{\text{SA}}^{(\text{out})} \epsilon_{\text{DAC}}(B_{\text{SA}})/N_{\text{SA}}$. As a consequence, the transmission noise is $\sigma_{n,\text{tx}}^2 = P_{\text{SA}}^{(\text{out})} N_{\text{SA}} \epsilon_{\text{DAC}}(B_{\text{DA}})/U^2$.

In FH architecture, the quantization noise from each DAC is amplified to $P_{\text{FH}}^{(\text{out})}/(NU)$ in each PA. As a result, the total transmitter noise power is $\sigma_{n,\text{tx}}^2 = P_{\text{FH}}^{(\text{out})} N_{\text{FH}} \sigma_{\text{DAC}}^2(B_{\text{FH}})/U$.

B. Impact of phase shifter quantization error and random error on beamforming gain

Consider a linear phased array system with N antenna elements that steers a beam towards direction γ in a 2D plane. Beamforming vector is given by $[e^{j\phi_1}, \dots, e^{j\phi_N}]$, where $\phi_n = (n-1)\pi \sin(\gamma)$. In the next, we derive beamforming gain at the main lobe for system with ideal and non-ideal phase shifters.

Let us denote the signal at the n^{th} elements as w_n with $|w_n| = 1/\sqrt{N}$, $\forall n$ when all phase shifters are ideal. Clearly, the phase shifter needs to be set such that signals are constructively added in the intended direction, i.e., $w_n e^{j\phi_n} = 1/\sqrt{N}$, and the beamforming gain is

$$G = \left| \sum_{n=1}^N w_n e^{j\phi_n} \right|^2 = N$$

When all phase shifters are non-ideal, the signal at the n^{th} element is denoted as $w'_n = w_n \exp(j\psi_n)$, where ψ_n is the phase error due to quantization and random implementation impairment. With Q bits quantization, the phase error ψ_n is bounded as $|\psi_n| \leq \epsilon$ where $\epsilon = \pi/2^Q$. The corresponding beamforming gain is

$$\begin{aligned} G' &= \left| \sum_{n=1}^N (w'_n e^{j\phi_n}) \right|^2 = \left| \sum_{n=1}^N (w_n e^{j\psi_n}) e^{j\phi_n} \right|^2 \\ &= \frac{1}{N} \left| \sum_{n=1}^N e^{j\psi_n} \right|^2 = \frac{1}{N} \left| \sum_{n=1}^N \cos(\psi_n) + j \sum_{n=1}^N \sin(\psi_n) \right|^2 \\ &= \frac{1}{N} \left[\sum_{n=1}^N \cos(\psi_n) \right]^2 + \frac{1}{N} \left[\sum_{n=1}^N \sin(\psi_n) \right]^2 \\ &\geq \frac{1}{N} \left[\sum_{n=1}^N \cos(\psi_n) \right]^2 \\ &\geq N \cos^2(\epsilon) \end{aligned}$$

where the second inequality is valid so long as $Q \geq 1$, i.e., $|\psi_n| \leq \pi/2, \forall n$.

Therefore the gain reduction is bounded by

$$10 \log_{10} \left[\frac{G}{G'} \right] \leq -20 \log_{10} \left[\cos \left(\frac{\pi}{2^Q} \right) \right] \text{ [dB]}$$

The above derivation shows that the gain drop in the main lobe is less than 0.68dB, 0.16dB and 0.04dB with $Q = 3$ to 5 bits quantization. Besides, these values are independent from the antenna size N . Equivalently, when phase shifter implementation error is less than $\epsilon = 22.5^\circ$, 11.25° , and 5.625° , gain drop is also bounded by 0.68dB, 0.16dB and 0.04dB, respectively.

REFERENCES

- [1] F. Boccardi, R. W. Heath, A. Lozano, T. L. Marzetta, and P. Popovski, "Five disruptive technology directions for 5G," *IEEE Commun. Mag.*, vol. 52, no. 2, pp. 74–80, Feb. 2014.
- [2] Z. Pi and F. Khan, "An introduction to millimeter-wave mobile broadband systems," *IEEE Commun. Mag.*, vol. 49, no. 6, pp. 101–107, Jun. 2011.
- [3] FCC, "Fact sheet: Spectrum frontiers proposal to identify, open up vast amounts of new high-band spectrum for next generation (5G) wireless broadband," Jul. 2016. [Online]. Available: https://apps.fcc.gov/edocs_public/attachmatch/DOC-339990A1.pdf
- [4] J. G. Andrews, S. Buzzi, W. Choi, S. V. Hanly, A. Lozano, A. C. K. Soong, and J. C. Zhang, "What will 5G be?" *IEEE J. Sel. Areas Commun.*, vol. 32, no. 6, pp. 1065–1082, Jun. 2014.
- [5] A. Ghosh, T. A. Thomas, M. C. Cudak, R. Ratasuk, P. Moorut, F. W. Vook, T. S. Rappaport, G. R. MacCartney, S. Sun, and S. Nie, "Millimeter-wave enhanced local area systems: A high-data-rate approach for future wireless networks," *IEEE J. Sel. Areas Commun.*, vol. 32, no. 6, pp. 1152–1163, Jun. 2014.
- [6] S. Rangan, T. S. Rappaport, and E. Erkip, "Millimeter-wave cellular wireless networks: Potentials and challenges," *Proc. IEEE*, vol. 102, no. 3, pp. 366–385, Mar. 2014.
- [7] T. S. Rappaport, S. Sun, R. Mayzus, H. Zhao, Y. Azar, K. Wang, G. N. Wong, J. K. Schulz, M. Samimi, and F. Gutierrez, "Millimeter wave mobile communications for 5G cellular: It will work!" *IEEE Access*, vol. 1, pp. 335–349, May 2013.
- [8] R. Baldemair, T. Irnich, K. Balachandran, E. Dahlman, G. Mildh, Y. Seln, S. Parkvall, M. Meyer, and A. Osseiran, "Ultra-dense networks in millimeter-wave frequencies," *IEEE Commun. Mag.*, vol. 53, no. 1, pp. 202–208, Jan. 2015.
- [9] N. Bhushan, J. Li, D. Malladi, R. Gilmore, D. Brenner, A. Damjanovic, R. T. Sukhvasi, C. Patel, and S. Geirhofer, "Network densification: the dominant theme for wireless evolution into 5G," *IEEE Commun. Mag.*, vol. 52, no. 2, pp. 82–89, Feb. 2014.
- [10] 3GPP, "LTE-Advanced," Jun. 2013. [Online]. Available: <http://www.3gpp.org/technologies/keywords-acronyms/97-lte-advanced>
- [11] C. Shepard, H. Yu, N. Anand, E. Li, T. Marzetta, R. Yang, and L. Zhong, "Argos: Practical many-antenna base stations," in *Proceedings of the 18th Annual International Conference on Mobile Computing and Networking*, ser. Mobicom '12, 2012, pp. 53–64. [Online]. Available: <http://doi.acm.org/10.1145/2348543.2348553>
- [12] F. Rusek, D. Persson, B. K. Lau, E. G. Larsson, T. L. Marzetta, O. Edfors, and F. Tufvesson, "Scaling up MIMO: Opportunities and challenges with very large arrays," *IEEE Signal Process. Mag.*, vol. 30, no. 1, pp. 40–60, Jan. 2013.
- [13] A. L. Swindlehurst, E. Ayanoglu, P. Heydari, and F. Capolino, "Millimeter-wave massive MIMO: the next wireless revolution?" *IEEE Commun. Mag.*, vol. 52, no. 9, pp. 56–62, Sep. 2014.
- [14] A. Alkhateeb, J. Mo, N. Gonzalez-Prelcic, and R. W. Heath, "MIMO precoding and combining solutions for millimeter-wave systems," *IEEE Commun. Mag.*, vol. 52, no. 12, pp. 122–131, Dec. 2014.
- [15] S. Han, C. I. I, Z. Xu, and C. Rowell, "Large-scale antenna systems with hybrid analog and digital beamforming for millimeter wave 5G," *IEEE Commun. Mag.*, vol. 53, no. 1, pp. 186–194, Jan. 2015.
- [16] J. S. Herd and M. D. Conway, "The evolution to modern phased array architectures," *Proc. IEEE*, vol. 104, no. 3, pp. 519–529, Mar. 2016.
- [17] X. Zhang, A. F. Molisch, and S.-Y. Kung, "Variable-phase-shift-based RF-baseband codesign for MIMO antenna selection," *IEEE Trans. Signal Process.*, vol. 53, no. 11, pp. 4091–4103, Nov. 2005.
- [18] R. W. Heath, N. Gonzalez-Prelcic, S. Rangan, W. Roh, and A. M. Sayeed, "An overview of signal processing techniques for millimeter wave MIMO systems," *IEEE J. Sel. Topics Signal Process.*, vol. 10, no. 3, pp. 436–453, Apr. 2016.
- [19] M. Xiao, S. Mumtaz, Y. Huang, L. Dai, Y. Li, M. Matthaiou, G. K. Karagiannis, E. Björnson, K. Yang, C. L. I, and A. Ghosh, "Millimeter wave communications for future mobile networks," *IEEE J. Sel. Areas Commun.*, vol. 35, no. 9, pp. 1909–1935, Sep. 2017.
- [20] A. F. Molisch, V. V. Ratnam, S. Han, Z. Li, S. L. H. Nguyen, L. Li, and K. Haneda, "Hybrid beamforming for massive MIMO: A survey," *IEEE Commun. Mag.*, vol. 55, no. 9, pp. 134–141, Sep. 2017.
- [21] S. Kuttu and D. Sen, "Beamforming for millimeter wave communications: An inclusive survey," *IEEE Commun. Surveys Tuts.*, vol. 18, no. 2, pp. 949–973, Secondquarter 2016.
- [22] 5GPPP, "D5.2 Final multi-node and multi-antenna transmitter and receiver architectures and schemes," Jun. 2017. [Online]. Available: <https://5g-mmmagic.eu/results/#deliverables>

- [23] A. Puglielli, A. Townley, G. LaCaille, V. Milovanovi, P. Lu, K. Trotskovsky, A. Whitcombe, N. Narevsky, G. Wright, T. Courtade, E. Alon, B. Nikoli, and A. M. Niknejad, "Design of energy- and cost-efficient massive MIMO arrays," *Proc. IEEE*, vol. 104, no. 3, pp. 586–606, Mar. 2016.
- [24] S. He, C. Qi, Y. Wu, and Y. Huang, "Energy-efficient transceiver design for hybrid sub-array architecture MIMO systems," *IEEE Access*, vol. 4, pp. 9895–9905, 2016.
- [25] X. Gao, L. Dai, S. Han, C. L. I, and R. W. Heath, "Energy-efficient hybrid analog and digital precoding for mmwave MIMO systems with large antenna arrays," *IEEE J. Sel. Areas Commun.*, vol. 34, no. 4, pp. 998–1009, Apr. 2016.
- [26] C. G. Tsinos, S. Maleki, S. Chatzinotas, and B. Ottersten, "On the energy-efficiency of hybrid analog-digital transceivers for single- and multi-carrier large antenna array systems," *IEEE J. Sel. Areas Commun.*, vol. 35, no. 9, pp. 1980–1995, Sep. 2017.
- [27] E. Bjrnson, M. Matthaiou, and M. Debbah, "Massive MIMO with non-ideal arbitrary arrays: Hardware scaling laws and circuit-aware design," *IEEE Trans. Wireless Commun.*, vol. 14, no. 8, pp. 4353–4368, Aug. 2015.
- [28] S. Mondal, R. Singh, A. I. Hussein, and J. Paramesh, "A 25-30 GHz 8-antenna 2-stream hybrid beamforming receiver for MIMO communication," in *2017 IEEE Radio Frequency Integrated Circuits Symposium (RFIC)*, Jun. 2017, pp. 112–115.
- [29] U. Kodak and G. M. Rebeiz, "Bi-directional flip-chip 28 GHz phased-array core-chip in 45nm CMOS SOI for high-efficiency high-linearity 5G systems," in *2017 IEEE Radio Frequency Integrated Circuits Symposium (RFIC)*, Jun. 2017, pp. 61–64.
- [30] J. Han, J. Kim, J. Park, and J. Kim, "A Ka-band 4-ch bi-directional CMOS T/R chipset for 5G beamforming system," in *2017 IEEE Radio Frequency Integrated Circuits Symposium (RFIC)*, Jun. 2017, pp. 41–44.
- [31] L. Wu, H. F. Leung, A. Li, and H. C. Luong, "A 4-element 60-GHz CMOS phased-array receiver with beamforming calibration," *IEEE Trans. Circuits Syst. I*, vol. 64, no. 3, pp. 642–652, Mar. 2017.
- [32] G. Mangraviti, K. Khalaf, Q. Shi, K. Vaesen, D. Guermandi, V. Giannini, S. Brebels, F. Frazzica, A. Bourdoux, C. Soens, W. V. Thillo, and P. Wambacq, "A 4-antenna-path beamforming transceiver for 60GHz multi-Gb/s communication in 28nm CMOS," in *2016 IEEE International Solid-State Circuits Conference (ISSCC)*, Jan. 2016, pp. 246–247.
- [33] M. Boers, B. Afshar, I. Vassiliou, S. Sarkar, S. T. Nicolson, E. Adabi, B. G. Perumana, T. Chalvatzi, S. Kavvadias, P. Sen, W. L. Chan, A. H. T. Yu, A. Parsa, M. Nariman, S. Yoon, A. G. Besoli, C. A. Kyriazidou, G. Zochios, J. A. Castaneda, T. Sowlati, M. Rofougaran, and A. Rofougaran, "A 16TX/16RX 60 GHz 802.11ad chipset with single coaxial interface and polarization diversity," *IEEE J. Solid-State Circuits*, vol. 49, no. 12, pp. 3031–3045, Dec. 2014.
- [34] E. Cohen, M. Ruberto, M. Cohen, O. Degani, S. Ravid, and D. Ritter, "A CMOS bidirectional 32-element phased-array transceiver at 60 GHz with LTCC antenna," *IEEE Trans. Microw. Theory Techn.*, vol. 61, no. 3, pp. 1359–1375, Mar. 2013.
- [35] B. Sadhu, Y. Tousi, J. Hallin, S. Sahl, S. Reynolds, . Renstrm, K. Sjgren, O. Haapalahti, N. Mazar, B. Bokinge, G. Weibull, H. Bengtsson, A. Carlinger, E. Westesson, J. E. Thillberg, L. Rexberg, M. Yeck, X. Gu, D. Friedman, and A. Valdes-Garcia, "A 28GHz 32-element phased-array transceiver IC with concurrent dual polarized beams and 1.4° beam-steering resolution for 5G communication," in *2017 IEEE International Solid-State Circuits Conference (ISSCC)*, Feb. 2017, pp. 128–129.
- [36] S. Zahir, O. D. Gurbuz, A. Karrooy, S. Raman, and G. M. Rebeiz, "A 60 GHz single-chip 256-element wafer-scale phased array with EIRP of 45 dBm using sub-reticle stitching," in *2015 IEEE Radio Frequency Integrated Circuits Symposium (RFIC)*, May 2015, pp. 23–26.
- [37] B. H. Ku, O. Inac, M. Chang, H. H. Yang, and G. M. Rebeiz, "A high-linearity 76 to 85-GHz 16-element 8-transmit/8-receive phased-array chip with high isolation and flip-chip packaging," *IEEE Trans. Microw. Theory Techn.*, vol. 62, no. 10, pp. 2337–2356, Oct. 2014.
- [38] A. Valdes-Garcia, A. Natarajan, D. Liu, M. Sanduleanu, X. Gu, M. Ferriss, B. Parker, C. Baks, J. O. Plouchart, H. Ainspan, B. Sadhu, M. Islam, and S. Reynolds, "A fully-integrated dual-polarization 16-element W-band phased-array transceiver in SiGe BiCMOS," in *2013 IEEE Radio Frequency Integrated Circuits Symposium (RFIC)*, Jun. 2013, pp. 375–378.
- [39] K. J. Maalouf and E. Lier, "Theoretical and experimental study of interference in multibeam active phased array transmit antenna for satellite communications," *IEEE Trans. Antennas Propag.*, vol. 52, no. 2, pp. 587–592, Feb. 2004.
- [40] M. Banu, "HDAAS: An efficient massive-MIMO technology," in *Brooklyn 5G Summit 2017*, 2017. [Online]. Available: <https://ieeetv.ieee.org/channels/communications>
- [41] A. S. Y. Poon and M. Taghivand, "Supporting and enabling circuits for antenna arrays in wireless communications," *Proc. IEEE*, vol. 100, no. 7, pp. 2207–2218, Jul. 2012.
- [42] B. Yang, Z. Yu, J. Lan, R. Zhang, J. Zhou, and W. Hong, "Digital beamforming-based massive MIMO transceiver for 5G millimeter-wave communications," *IEEE Trans. Microw. Theory Techn.*, vol. 66, no. 7, pp. 3403–3418, Jul. 2018.
- [43] R. Mndez-Rial, C. Rusu, N. Gonzalez-Prelcic, A. Alkhateeb, and R. W. Heath, "Hybrid MIMO architectures for millimeter wave communications: Phase shifters or switches?" *IEEE Access*, vol. 4, pp. 247–267, 2016.
- [44] J. Brady, N. Behdad, and A. M. Sayeed, "Beamspace MIMO for millimeter-wave communications: System architecture, modeling, analysis, and measurements," *IEEE Trans. Antennas Propag.*, vol. 61, no. 7, pp. 3814–3827, Jul. 2013.
- [45] 5GPPP, "D1.1 use case characterization, KPIs and preferred suitable frequency ranges for future 5G systems between 6 GHz and 100 GHz," Nov. 2017. [Online]. Available: <https://5g-mmmagic.eu/results/#deliverables>
- [46] 3GPP, "TR 38.913 Study on scenarios and requirements for next generation access technologies," Sep. 2016. [Online]. Available: <http://www.3gpp.org/DynaReport/38913.htm>
- [47] Z. Pi, J. Choi, and R. Heath, "Millimeter-wave gigabit broadband evolution toward 5G: fixed access and backhaul," *IEEE Commun. Mag.*, vol. 54, no. 4, pp. 138–144, Apr. 2016.
- [48] 3GPP, "TR 38.900 Study on channel model for frequency spectrum above 6 GHz," Jul. 2017. [Online]. Available: <http://www.3gpp.org/DynaReport/38900.htm>
- [49] Y. Azar, G. N. Wong, K. Wang, R. Mayzus, J. K. Schulz, H. Zhao, F. Gutierrez, D. Hwang, and T. S. Rappaport, "28 GHz propagation measurements for outdoor cellular communications using steerable beam antennas in New York city," in *2013 IEEE International Conference on Communications (ICC)*, Jun. 2013, pp. 5143–5147.
- [50] C. B. Peel, B. M. Hochwald, and A. L. Swindlehurst, "A vector-perturbation technique for near-capacity multiantenna multiuser communication-part I: channel inversion and regularization," *IEEE Trans. Commun.*, vol. 53, no. 1, pp. 195–202, Jan. 2005.
- [51] A. Alkhateeb, G. Leus, and R. W. Heath, "Limited feedback hybrid precoding for multi-user millimeter wave systems," *IEEE Trans. Wireless Commun.*, vol. 14, no. 11, pp. 6481–6494, Nov. 2015.
- [52] Y. Ghasempour, C. R. C. M. da Silva, C. Cordeiro, and E. W. Knightly, "IEEE 802.11ay: Next-generation 60 GHz communication for 100 Gb/s Wi-Fi," *IEEE Commun. Mag.*, vol. 55, no. 12, pp. 186–192, Dec. 2017.
- [53] H. Jin, W. Che, K. S. Chin, G. Shen, W. Yang, and Q. Xue, "60-GHz LTCC differential-fed patch antenna array with high gain by using soft-surface structures," *IEEE Trans. Antennas Propag.*, vol. 65, no. 1, pp. 206–216, Jan. 2017.
- [54] A. Natarajan, S. K. Reynolds, M. D. Tsai, S. T. Nicolson, J. H. C. Zhan, D. G. Kam, D. Liu, Y. L. O. Huang, A. Valdes-Garcia, and B. A. Floyd, "A fully-integrated 16-element phased-array receiver in SiGe BiCMOS for 60-GHz communications," *IEEE J. Solid-State Circuits*, vol. 46, no. 5, pp. 1059–1075, May 2011.
- [55] S. Zahir, O. D. Gurbuz, A. Kar-Roy, S. Raman, and G. M. Rebeiz, "60-GHz 64- and 256-elements wafer-scale phased-array transmitters using full-reticle and subreticle stitching techniques," *IEEE Trans. Microw. Theory Techn.*, vol. 64, no. 12, pp. 4701–4719, Dec. 2016.
- [56] G. Auer, V. Giannini, C. Desset, I. Godor, P. Skillermark, M. Olsson, M. A. Imran, D. Sabella, M. J. Gonzalez, O. Blume, and A. Fehske, "How much energy is needed to run a wireless network?" *IEEE Wireless Commun.*, vol. 18, no. 5, pp. 40–49, Oct. 2011.
- [57] 3GPP, "NR: Overall description; Stage-2, 3rd generation partnership project (3GPP), TS 38.300," Dec. 2017. [Online]. Available: <http://www.3gpp.org/DynaReport/38300.htm>
- [58] F.-L. Yuan and D. Markovi, "A 13.1gops/mw 16-core processor for software-defined radios in 40nm cmos," in *2014 Symposium on VLSI Circuits Digest of Technical Papers*, Jun. 2014, pp. 1–2.
- [59] D. Cui, H. Zhang, N. Huang, A. Nazemi, B. Catli, H. G. Rhew, B. Zhang, A. Momtaz, and J. Cao, "3.2 A 320mW 32Gb/s 8b ADC-based PAM-4 Analog Front-End with Programmable Gain Control and Analog Peaking in 28nm CMOS," in *2016 IEEE International Solid-State Circuits Conference (ISSCC)*, Jan. 2016.
- [60] A. Nazemi, K. Hu, B. Catli, D. Cui, U. Singh, T. He, Z. Huang, B. Zhang, A. Momtaz, and J. Cao, "A 36Gb/s PAM4 transmitter using

- an 8b 18Gs/s DAC in 28nm CMOS,” in *2015 IEEE International Solid-State Circuits Conference - (ISSCC) Digest of Technical Papers*, Feb. 2015, pp. 1–3.
- [61] M. Ferriss, B. Sadhu, A. Rylyakov, H. Ainspan, and D. Friedman, “A 13.1-to-28GHz fractional-N PLL in 32nm SOI CMOS with a Delta-Sigma noise-cancellation scheme,” in *2015 IEEE International Solid-State Circuits Conference - (ISSCC) Digest of Technical Papers*, Feb. 2015, pp. 1–3.
- [62] S. Ek, T. Phlsson, A. Carlsson, A. Axhult, A. K. Stenman, and H. Sjlund, “A 16-20 GHz LO system with 115 fs jitter for 24-30 GHz 5G in 28 nm FD-SOI CMOS,” in *ESSCIRC 2017 - 43rd IEEE European Solid State Circuits Conference*, Sep. 2017, pp. 251–254.
- [63] W. El-Halwagy, A. Nag, P. Hisayasu, F. Aryanfar, P. Mousavi, and M. Hossain, “A 28GHz quadrature fractional-N synthesizer for 5G mobile communication with less than 100fs jitter in 65nm CMOS,” in *2016 IEEE Radio Frequency Integrated Circuits Symposium (RFIC)*, May 2016, pp. 118–121.
- [64] M. Ferriss, A. Rylyakov, J. A. Tierno, H. Ainspan, and D. J. Friedman, “A 28 GHz hybrid PLL in 32 nm SOI CMOS,” *IEEE J. Solid-State Circuits*, vol. 49, no. 4, pp. 1027–1035, Apr. 2014.
- [65] R. Krishnan, M. R. Khanzadi, N. Krishnan, Y. Wu, A. G. i Amat, T. Eriksson, and R. Schober, “Linear massive MIMO precoders in the presence of phase noise: A large-scale analysis,” vol. 65, no. 5, pp. 3057–3071, May 2016.
- [66] R. Garg and A. S. Natarajan, “A 28-GHz low-power phased-array receiver front-end with 360° RTPS phase shift range,” *IEEE Trans. Microw. Theory Techn.*, vol. 65, no. 11, pp. 4703–4714, Nov. 2017.
- [67] G. S. Shin, J. S. Kim, H. M. Oh, S. Choi, C. W. Byeon, J. H. Son, J. H. Lee, and C. Y. Kim, “Low insertion loss, compact 4-bit phase shifter in 65 nm CMOS for 5G applications,” *IEEE Microwave and Wireless Components Letters*, vol. 26, no. 1, pp. 37–39, Jan. 2016.
- [68] F. Meng, K. Ma, K. S. Yeo, and S. Xu, “A 57-to-64-GHz 0.094-mm² 5-bit passive phase shifter in 65-nm CMOS,” *IEEE Trans. VLSI Syst.*, vol. 24, no. 5, pp. 1917–1925, May 2016.
- [69] W. Shin and G. M. Rebeiz, “60 GHz active phase shifter using an optimized quadrature all-pass network in 45nm CMOS,” in *2012 IEEE/MTT-S International Microwave Symposium Digest*, Jun. 2012, pp. 1–3.
- [70] S. Shakib, M. Elkholy, J. Dunworth, V. Aparin, and K. Entesari, “A wideband 28GHz power amplifier supporting 8 by 100MHz carrier aggregation for 5G in 40nm CMOS,” in *2017 IEEE International Solid-State Circuits Conference (ISSCC)*, Feb. 2017, pp. 44–45.
- [71] B. Moret, V. Knopik, and E. Kerherve, “A 28GHz self-contained power amplifier for 5G applications in 28nm FD-SOI CMOS,” in *2017 IEEE 8th Latin American Symposium on Circuits Systems (LASCAS)*, Feb. 2017, pp. 1–4.
- [72] S. Shakib, H. C. Park, J. Dunworth, V. Aparin, and K. Entesari, “A highly efficient and linear power amplifier for 28-GHz 5G phased array radios in 28-nm CMOS,” *IEEE J. Solid-State Circuits*, vol. 51, no. 12, pp. 3020–3036, Dec. 2016.
- [73] B. Park, S. Jin, D. Jeong, J. Kim, Y. Cho, K. Moon, and B. Kim, “Highly linear mm-Wave CMOS power amplifier,” *IEEE Trans. Microw. Theory Techn.*, vol. 64, no. 12, pp. 4535–4544, Dec. 2016.
- [74] A. Sarkar and B. A. Floyd, “A 28-GHz harmonic-tuned power amplifier in 130-nm SiGe BiCMOS,” *IEEE Trans. Microw. Theory Techn.*, vol. 65, no. 2, pp. 522–535, Feb. 2017.
- [75] A. Sarkar, F. Aryanfar, and B. A. Floyd, “A 28-GHz SiGe BiCMOS PA with 32% efficiency and 23-dBm output power,” *IEEE J. Solid-State Circuits*, vol. 52, no. 6, pp. 1680–1686, Jun. 2017.
- [76] K. Kim and C. Nguyen, “A 16.5 to 28 GHz 0.18-um BiCMOS power amplifier with flat 19.4 pm 1.2 dBm output power,” *IEEE Microwave and Wireless Components Letters*, vol. 24, no. 2, pp. 108–110, Feb. 2014.
- [77] D. P. Nguyen, B. L. Pham, and A. V. Pham, “A compact 29% PAE at 6 dB power back-off E-mode GaAs pHEMT MMIC doherty power amplifier at Ka-band,” in *2017 IEEE MTT-S International Microwave Symposium (IMS)*, Jun. 2017, pp. 1683–1686.
- [78] Qorvo, “Datasheet of TGA4544-SM.” [Online]. Available: <http://www.qorvo.com/products/p/TGA4544-SM>
- [79] Analog-Devices, “Datasheet of HMC1132.” [Online]. Available: <http://www.analog.com/en/products/rf-microwave/rf-amplifiers/power-amplifiers/hmc1132.html/product-overview>
- [80] K. Fujii, “Low cost Ka-band 7W GaAs PHEMT based HPA with GaN PHEMT equivalent performance,” in *2015 IEEE Radio Frequency Integrated Circuits Symposium (RFIC)*, May 2015, pp. 207–210.
- [81] S. Din, M. Wojtowicz, and M. Siddiqui, “High power and high efficiency Ka band power amplifier,” in *2015 IEEE MTT-S International Microwave Symposium*, May 2015, pp. 1–4.
- [82] Y. Frans, S. McLeod, H. Hedayati, M. Elzeftawi, J. Namkoong, W. Lin, J. Im, P. Upadhyaya, and K. Chang, “3.7 A 40-to-64Gb/s NRZ transmitter with supply-regulated front-end in 16nm FinFET,” in *2016 IEEE International Solid-State Circuits Conference (ISSCC)*, Jan. 2016, pp. 68–70.
- [83] Ericsson, “Ericsson mobility report,” Nov. 2017. [Online]. Available: <https://www.ericsson.com/assets/local/mobility-report/documents/2017/ericsson-mobility-report-november-2017.pdf>
- [84] R. Ho, K. W. Mai, and M. A. Horowitz, “The Future of Wires,” *Proc. IEEE*, vol. 89, no. 4, pp. 490–504, Apr. 2001.
- [85] A. Pitarokoilis, E. Bjrnson, and E. G. Larsson, “Performance of the massive MIMO uplink with OFDM and phase noise,” *IEEE Commun. Lett.*, vol. 20, no. 8, pp. 1595–1598, Aug. 2016.
- [86] W. B. Abbas, F. Gomez-Cuba, and M. Zorzi, “Millimeter wave receiver efficiency: A comprehensive comparison of beamforming schemes with low resolution ADCs,” *IEEE Trans. Wireless Commun.*, vol. 16, no. 12, pp. 8131–8146, Dec. 2017.
- [87] K. Roth, H. Pirzadeh, A. L. Swindlehurst, and J. A. Nossek, “A comparison of hybrid beamforming and digital beamforming with low-resolution ADCs for multiple users and imperfect CSI,” *IEEE J. Sel. Topics Signal Process.*, vol. 12, no. 3, pp. 484–498, Jun. 2018.
- [88] C. K. Wen, C. J. Wang, S. Jin, K. K. Wong, and P. Ting, “Bayes-optimal joint channel-and-data estimation for massive MIMO with low-precision ADCs,” *IEEE Trans. Signal Process.*, vol. 64, no. 10, pp. 2541–2556, May 2016.
- [89] J. Mo, A. Alkhateeb, S. Abu-Surra, and R. W. Heath, “Hybrid architectures with few-bit ADC receivers: Achievable rates and energy-rate tradeoffs,” *IEEE Trans. Wireless Commun.*, vol. 16, no. 4, pp. 2274–2287, Apr. 2017.